Recent Developments in Chemical Vapor Deposition of 2D Magnetic Transition Metal Chalcogenides

Bijun Tang[†,‡], *Dianyi Hu*[†,‡], *Xiaoxu Zhao*[†], *Xiaowei Wang*[†◇]*, *and Zheng Liu*[†,§,#,]*

[†]School of Materials Science and Engineering, Nanyang Technological University, Singapore 639798, Singapore

[◇] i-Lab, Key Laboratory of Multifunctional Nanomaterials and Smart Systems, Suzhou Institute of NanoTech and Nano-Bionics, Chinese Academy of Sciences, Suzhou 215123, China

[§]CINTRA CNRS/NTU/THALES, UMI 3288, Research Techno Plaza, 50 Nanyang Drive, Border X Block, Level 6, Singapore 637553, Singapore

[#]School of Electrical and Electronic Engineering, Nanyang Technological University, Singapore, 639798, Singapore

[‡]These authors contributed equally to this work.

* Email: wangxiaowei@ntu.edu.sg, z.liu@ntu.edu.sg

Keywords: two-dimensional material, transition metal chalcogenides, chemical vapor deposition, magnetic property, crystal structure, stability

Abstract

In recent years, two-dimensional (2D) magnetic transition metal chalcogenides (TMCs) have attracted tremendous research interests thanks to their intriguing properties that are essential in developing future electronic and spintronic devices in this modernizing era. This review aims to introduce recent developments in the preparation of 2D magnetic TMCs, especially chromium and iron-based chalcogenides, their structures, as well as the related intriguing magnetic phenomena. Firstly, the common crystal structures of magnetic TMCs including both layered and non-layered structures are introduced. Various chemical vapor deposition strategies for synthesizing 2D magnetic TMCs are then introduced with emphasis on the key synthesis parameters. Moreover, the intriguing physical properties associated with 2D TMCs such as magnetic anisotropy, thickness and phase-dependent magnetic response as well as stability are summarized. Last but not least, challenges and future research directions are briefly discussed in light of recent advances in the field.

1. Introduction

Since the discovery of graphene, the family of two-dimensional (2D) materials has been growing rapidly in the past decades, enriched with a broad range of fascinating properties.[1-8] However, as an indispensable member of the 2D family, the development of 2D magnets is still in its infancy, hindered by the suppression of long-range magnetic order by thermal fluctuation in 2D systems.[9, 10] The breakthrough occurred in 2017, when 2D magnetism was first clearly confirmed in atomically thin CrI_3 and $CrGeTe_3$.[11, 12] This ground-breaking finding has immediately triggered substantial research interest, and ferromagnetism in 2D Fe_3GeTe_2 (FGT) was soon reported in 2018.[13, 14] Although these 2D magnets have demonstrated fascinating behaviors, such as layer-dependent magnetism in CrI_3[11] and room-temperature

ferromagnetism in FGT with ionic gating,[14] most of the available 2D magnets are unstable and obtained by mechanical exfoliation,[12-18] which is not only time-consuming, but also lack of control over the sample size and thickness, hindering their further study and application. 2D magnets are ideal candidates for exploring novel physical phenomena such as anomalous Hall effect, quantum Hall effect, and topological Hall effect, as well as promoting the realization of spintronics. The development of large-size uniform 2D magnets is therefore urgently required.[19]

With recent advances in the controllable chemical vapor deposition (CVD) of transition metal chalcogenides (TMCs),[20-27] exploration of CVD-grown magnetic TMCs has recently attracted substantial research attention. Compared with other synthesis methods, attributes of CVD such as large scale, high quality, and great tunability, renders CVD approaches gradually become the dominant method for preparing various kinds of 2D materials.[28-32] Compared with other 2D materials, TMCs with the general formula of M_aX_b (where M refers to a transition metal and X represents a chalcogen) exhibit rich structures and versatile properties,[1, 3, 20, 33-36] which thus provides an ideal platform for exploring 2D magnetism. Up to now, remarkable progress has been achieved with the study on 2D magnetic TMCs,[37-46] especially the chromium (Cr), iron (Fe), vanadium (V), and manganese (Mn)-based chalcogenides (Cr_mX_n, Fe_mX_n, V_mX_n, and Mn_mX_n), where ultrathin flakes with controllable phase and thickness have been successfully synthesized and the associated magnetic properties have been systematically studied. For instance, researchers have found out that by controlling the growth temperature, 2D FeTe in different phases (i.e., tetragonal vs. hexagonal) can be selectively prepared, demonstrating distinct magnet responses (i.e., antiferromagnetism vs. ferromagnetism).[39] It is worth mentioning, Cr and Fe are widely chosen attributed to their half-filled 3d orbitals, which are prone to giving rise to magnetic behaviors. In fact, not only chalcogenides, but interesting magnetic behaviors have also been reported in their phosphorus chalcogenides (e.g., intrinsic

antiferromagnetism in atomically thin $FePS_3$ and ferromagnetism in monolayer $CrPS_4$) and elemental forms (e.g., room-temperature ferromagnetism in ironene).[47-49]

This Review endeavors to provide an update-to-date overview of the recent progress in the CVD synthesis of magnetic 2D TMCs and the study of the associated structures and properties (Figure 1). Cr_mX_n and Fe_mX_n are especially focused, while V_mX_n and Mn_mX_n are briefly introduced. The structures of magnetic 2D TMCs, including both layered and non-layered structures, are first introduced. The role played by each key synthesis parameter in the formation of CVD-grown 2D magnetic TMCs is then summarized and discussed. In addition, the intriguing magnetic properties of 2D TMCs, such as thickness and phase dependency, are highlighted. Other essential properties, including electronic properties and stability, are briefly discussed as well. Finally, the prospects for future research on 2D magnetic TMCs are offered.

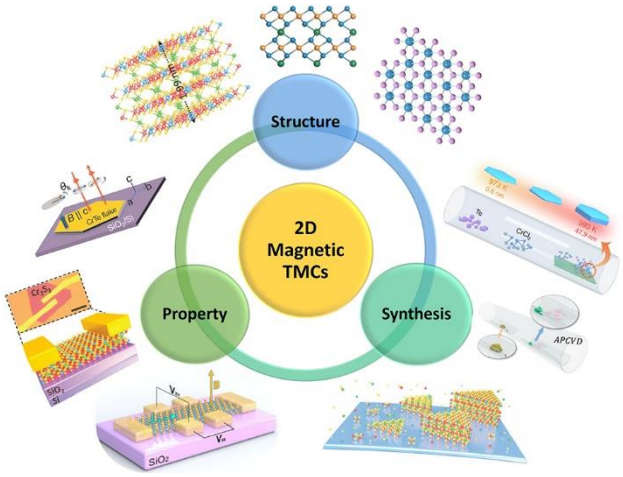

Figure 1. Overview of this review including structure, synthesis, and property of magnetic 2D TMCs. Reproduced with permission from ref 41, 50-54. Copyright 2019. Wiley-VCH.[41] Copyright 2019, American Chemical Society.[50] Copyright 2021, Springer Nature.[51] Copyright 2019. Wiley-VCH.[52] Copyright 2022, Springer Nature.[53] Copyright 2020, The Royal Society of Chemistry.[54]

2. Structures of 2D magnetic TMCs

Chromium chalcogenides (Cr_mX_n, X = S, Se, and Te) are recently emerging as a class of key materials due to their intriguing stoichiometry or composition-dependent magnetic properties. Cr_mX_n possesses a large number of binary compounds with various component ratios, such as Cr_2S_3,[41, 50, 55] CrSe,[52] $CrSe_2$,[40] CrTe,[54] Cr_2Te_3,[56, 57] Cr_5Te_8,[53, 58] and $CrTe_2$.[51] CrX_2 shares similar layered structures with the well-known transition metal dichalcogenides (e.g., MoS_2, WTe_2), whereas the rest stoichiometric Cr_mX_n reveals non-layered structures, which can be regarded as a self-intercalated compound with inserting additional Cr atoms into the van der Waals gap of CrX_2. For instance, Cr_2S_3 can be described as a stacking of alternating occupied CrS_2 layer and $Cr_{1/3}$ atom plane (coupled by strong covalent interaction) (Figure 2a),[50] CrSe can be viewed to be two $CrSe_2$ layers stacked together by sharing a layer of Se atoms (Figure 2b),[52] and Cr_5Te_8 can be considered as Cr atoms intercalated into $CrTe_2$ layers (Figure 2c). [58] Generally, the concentration and associated topology of the intercalated Cr atoms play vital roles in determining the structure and magnetic properties of Cr_mX_n. Because the structure-property relationship is central to materials science, identifying crystal structures at the atomic scale is critical towards the in-depth understanding and potential application of novel functional materials.

Annular dark-field scanning transmission electron microscopy (ADF-STEM) has been well adopted to unravel the atomic structure of the CVD-grown Cr_mX_n crystals. The contrast of the ADF-STEM image depends on the Z atomic number, which is around $Z^{1.6–1.7}$,[59, 60] thereby it is commonly employed to distinguish the polymorphism and local topological defects in 2D materials. However, there are many analogous compounds with slightly different stoichiometries sharing similar structures. Thus, precisely differentiating each unique Cr_mX_n phase is challenging. Extensive structural studies, such as quantitative STEM image analysis and image simulation, are required. For instance, Cui et al. have devoted great effort to determine whether the structure of their CVD-grown Cr_2S_3 is rhombohedral or trigonal (Figure

2d).[41] The comprehensive simulation was demonstrated to be effective in differentiating these rather similar degenerate phases. In the simulated rhombohedral phase, the contrast of Cr atom blobs is indiscernible at all atomic positions, agreeing well with the experimental Z contrast image. However, clear intensity reduction of Cr atoms blobs was identified in the trigonal phase in every $\sqrt{3}a \times \sqrt{3}a$. The intensity difference was attributed to different periodic stacking orders of $Cr_{1/3}$ atom plane, i.e., abc stacking in the rhombohedral phase whereas ab stacking in the trigonal phase. A similar strategy was also adopted by Li et al. to identify CVD-grown Cr-Se compound.[40] Intensity line profiles from simulated STEM images of rhombohedral phase (R-Cr_2Se_3), trigonal phase (T-Cr_2Se_3), and CrSe were systematically compared with experimental results (Figure 2e). The CVD-grown material was unambiguously determined to be $CrSe_2$. Very recently, by precisely examining ADF-STEM image and intensity line profiles, differentiation of trigonal and monoclinic Cr_5Te_8 was achieved (Figure 2f-g).[53] The atom-resolved structures play essential roles in understanding the phase-dependent magnetic properties, which will be discussed in the later parts.

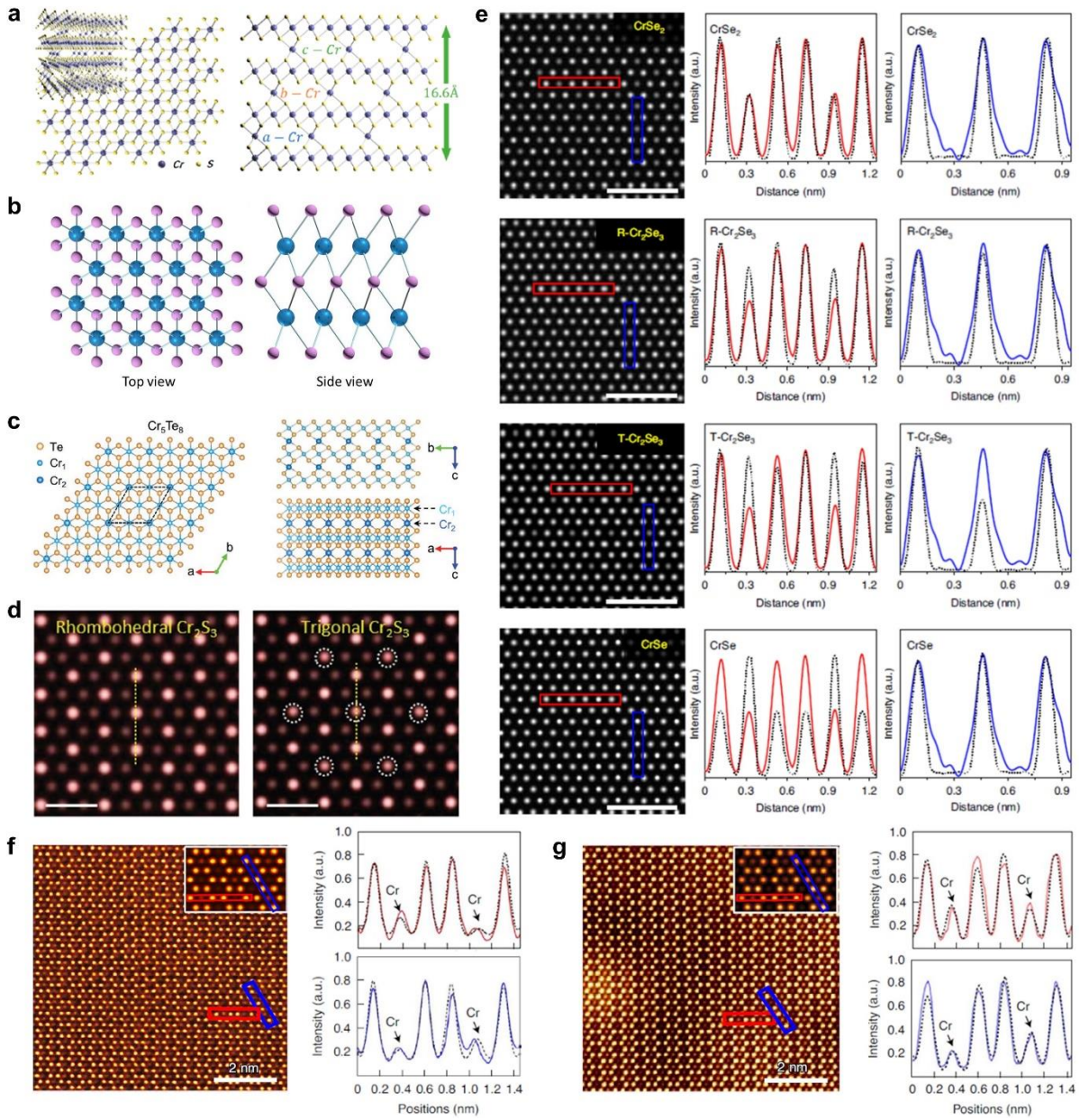

Figure 2. (a) Atomic structure of rhombohedral Cr_2S_3 nanosheets. Reproduced with permission from ref 50. Copyright 2019, American Chemical Society.[50] (b) Atomic model of hexagonal CrSe nanocrystals. Reproduced with permission from ref 52. Copyright 2019. Wiley-VCH.[52] (c) Structural model of trigonal Cr_5Te_8 flakes. Reproduced with permission from ref 58. Copyright 2021. Wiley-VCH.[58] (d) Simulated STEM images of the rhombohedral and trigonal Cr_2S_3 along the [001] direction. Scale bar: 0.5 nm. Reproduced with permission from ref 41. Copyright 2019. Wiley-VCH.[41] (e) Simulated STEM images and intensity line profiles of $CrSe_2$, R-Cr_2Se_3, T-Cr_2Se_3, and CrSe along [001] direction. Scale bar: 1 nm. Reproduced with permission from ref 40. Copyright 2021, Springer Nature.[40] (f-g) Simulated STEM images and intensity line profiles of trigonal and monoclinic Cr_5Te_8, respectively. Reproduced with permission from ref 53. Copyright 2022, Springer Nature.[53]

Similar to Cr_mX_n, the phase diagram of iron chalcogenides (Fe_mX_n) is also quite complicated. There are a variety of unique stoichiometric ratios, such as FeSe, $FeSe_2$, Fe_3Se_4, Fe_7Se_8, FeTe, and $FeTe_2$.[61-65] Even in the same composition, multiple phases could exist,[66] for example, hexagonal and tetragonal FeTe.[39, 67, 68] The complicated structures in the iron chalcogenides form the basis of rich magnetic properties, where the exchange function between the iron ions can be altered in different structures. So far, only Fe_7Se_8, $FeSe_2$, FeTe, and $FeTe_2$ have been prepared by the current solid-precursor-based CVD method.[39, 42, 69-75] Hexagonal $FeSe_2$ and $FeTe_2$ are layered materials, where each Fe atom plane is sandwiched by two Se or Te atom plains (Figure 3a-d).[69, 72] Besides, tetragonal FeTe also adopts layered structures, which comply with a P_{4g} wallpaper group symmetry, as shown in the atomic model and zoom-in STEM image in Figure 3e-i. The rest, including Fe_7Se_8 and hexagonal FeTe, are all intrinsically non-layered materials (Figure 3j-n).[39, 42] The CVD method enables the preparation of ultrathin non-layered nanomaterials, making it possible to study the thickness-dependence of magnetic properties in these materials. It should be noted that the "self-intercalated" phase may also exist in the layered iron chalcogenides.[73, 76] One example is that the superlattice FeTe phase was unveiled by STEM (Figure 3o-s).[73] This kind of structure could exist locally in CVD products. The intercalated iron ions possibly exhibit distinct magnetic order and change the magnetic properties of the material.

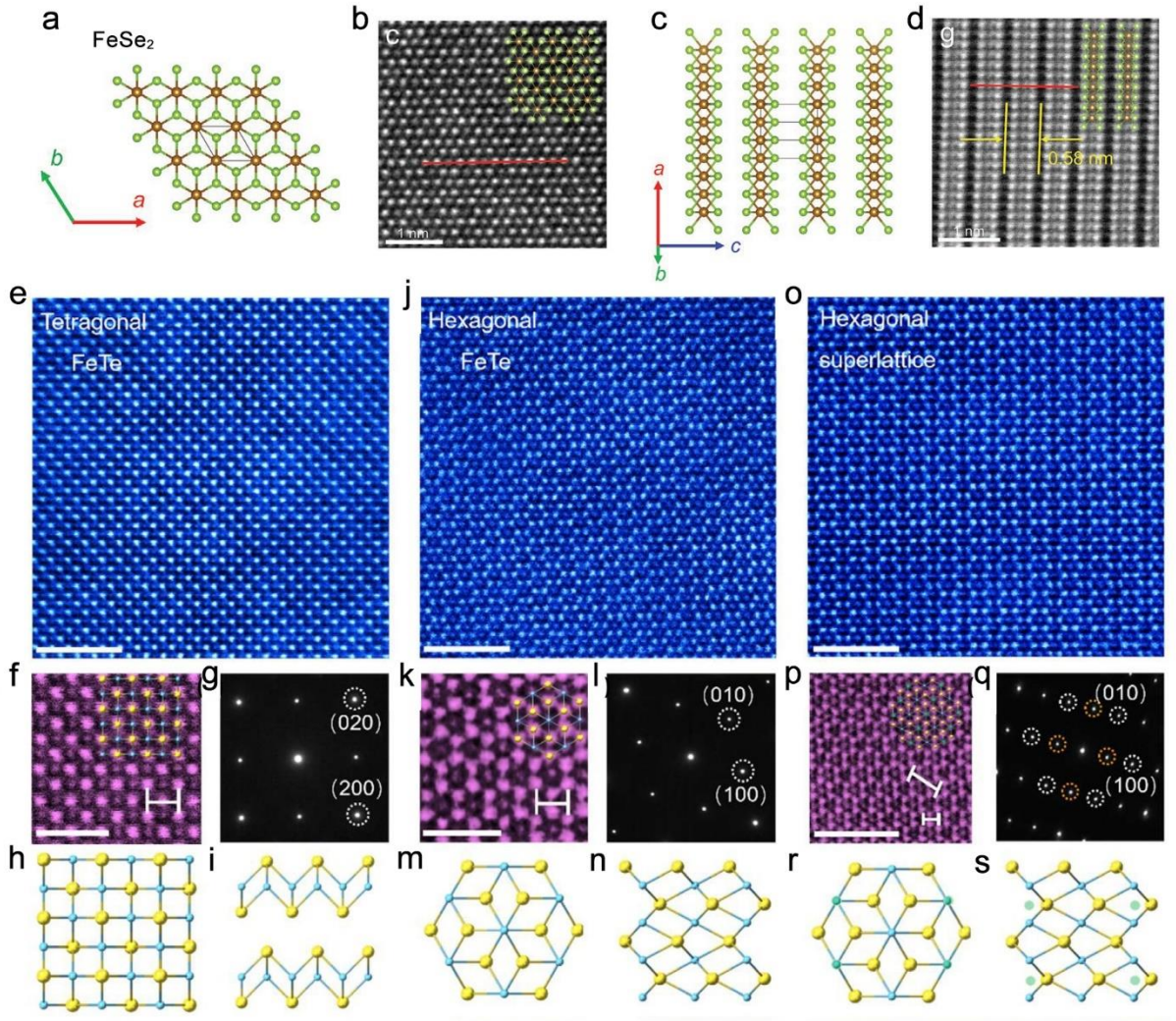

Figure 3. (a-d) Atomic models and ADF-STEM images of as-grown $FeSe_2$ nanocrystals: (a, b) Top and (c, d) side views of the layered $FeSe_2$. Reproduced with permission from ref 72. Copyright 2021, Wiley-VCH.[72] (e-s) The ADF-STEM images and atomic models of (e-i) tetragonal FeTe, (j-n) hexagonal FeTe, and (o-s) hexagonal FeTe with superlattice structure: (e, j, o) ADF-STEM images; (f, k, p) Enlarged ADF-STEM images and (g, l, q) the corresponding selected area electron diffraction (SAED) results; The simulated crystal model of the three characterized phases of FeTe from (h, m, r) the top view and (i, n, s) the side view. The blue and yellow balls stand for iron and tellurium atoms, respectively. Besides, the green balls (r, s) represent the anchored Fe atoms which may result in the superlattice structure. Reproduced with permission from ref 73. Copyright 2021, Elsevier.[73] Scale bar: (e, j, o) 2 nm; (f, k, p) 1 nm.

3. Synthesis of 2D magnetic TMCs

Owing to the abundant structures and associated versatile properties, composition and phase-controlled synthesis of magnetic 2D TMCs are therefore of great importance to meet targeted requirements. As mentioned earlier, over the past few years, CVD method has become a powerful tool for the reliable production of high-quality large-scale 2D TMCs. CVD is a chemical process containing multiple variables. In a typical CVD process, the silicon wafer, mica, or sapphire is generally used as the substrate. Liquid or solid precursors are used, which react at high temperatures in the gas state. The reaction typically takes place on the substrate or before reaching the substrate, and then the as-formed products will deposit onto the substrate. A carrier gas is required throughout the whole CVD process to constantly bring in the precursors and expel the reacted byproduct; sometimes, it may also promote the synthesis by taking part in the reaction. Rational design and careful tuning of the CVD growth processes are essential to the controllable growth of magnetic 2D TMCs.

The main achievements in the preparation of magnetic TMCs, including Cr_mX_n, Fe_mX_n, V_mX_n, and Mn_mX_n, are summarized in Table 1. The following parts will provide more discussions about the synthesis strategies adopted by the community to achieve the successful and controllable synthesis of intriguing magnetic TMCs.

3.1 CVD-Grown Chromium Chalcogenides (Cr_mX_n)

Cr_mX_n was reported to possess various magnetic properties, depending sensitively on the compositions and structures. However, preparation of most 2D Cr_mX_n remains challenging due to their non-layered nature, especially with the conventional exfoliation method. Great effort has been devoted by the community, and inspiringly, some advancements with CVD methods have been made recently. Here the key factors governing the successful synthesis of CVD-grown Cr_mX_n will be introduced, and some representative works will be discussed in detail.

3.1.1 Selection of Precursors

Metal oxides are one of the most commonly used precursors for the preparation of 2D TMCs. For instance, the well-studied monolayer MoX_2 and WX_2 (X=S, Se, Te) are generally prepared by the sulfuration/selenization/tellurization of MoO_3 and WO_3, respectively.[77-83] However, chromium oxide (i.e., Cr_2O_3), is not an ideal candidate for synthesizing Cr_mX_n owing to its extremely high melting point (m.p.) of 2435℃, which is hard to be evaporated under conventional CVD conditions.[55] Searching for more suitable precursors with moderate evaporation rate is therefore critical towards the successful synthesis of 2D Cr_mX_n.

Chromium halides, $CrCl_2$ (m.p. 824℃) and $CrCl_3$ (m.p. 1152℃), with lower melting points and higher saturated vapor pressure, are promising candidates for CVD growth. In the past few years, various 2D Cr_mX_n have been synthesized by sulfurization/selenization/tellurization of chromium halides, including Cr_2S_3, CrSe, $CrSe_2$, CrTe, Cr_2Te_3, Cr_3Te_4, Cr_5Te_8, and $CrTe_2$.[40, 50-52, 54, 55, 57, 58, 84] For instance, Zhou and his colleagues reported the CVD-grown of 2D Cr_2S_3 for the first time in 2018, with $CrCl_2$ and S serving as precursors.[55] The optical image of the grown Cr_2S_3 is shown in Figure 4a, whose ultrathin nature is confirmed by the corresponding atomic force microscopy (AFM) image (Figure 4b). Compared to $CrCl_2$, $CrCl_3$ appears to be an even more popular choice, as listed in Table 1. Its slightly higher melting point can guarantee the moderate feeding of the Cr precursors, which is conducive to the experimental controllability.

Although numerous Cr_mX_n have been synthesized from chromium halides, researchers are still searching for new precursors, as the sensitivity of $CrCl_2$ and $CrCl_3$ powders to moisture and air may affect the repeatability and increase the difficulty of experiments. Using the mixture of Cr and NaCl as the metal precursor, Cui and co-workers demonstrated the growth of nanometer-thick Cr_2S_3 flakes, whose OM and AFM images are shown in Figure 4c-d.[41] Although Cr has a relatively higher melting point of 1890℃, the addition of NaCl can sufficiently lower its

melting point and facilitate its volatilization at a relatively low temperature,[20, 85] promoting the growth of 2D Cr_2S_3. Furthermore, Na^+ ions also act as an efficient catalyst for reducing the energy barrier for the growth of TMCs.[86] Apart from Cr_2S_3, the salt-assisted method has been widely applied by the community to grow a large number of TMCs.[20, 87]

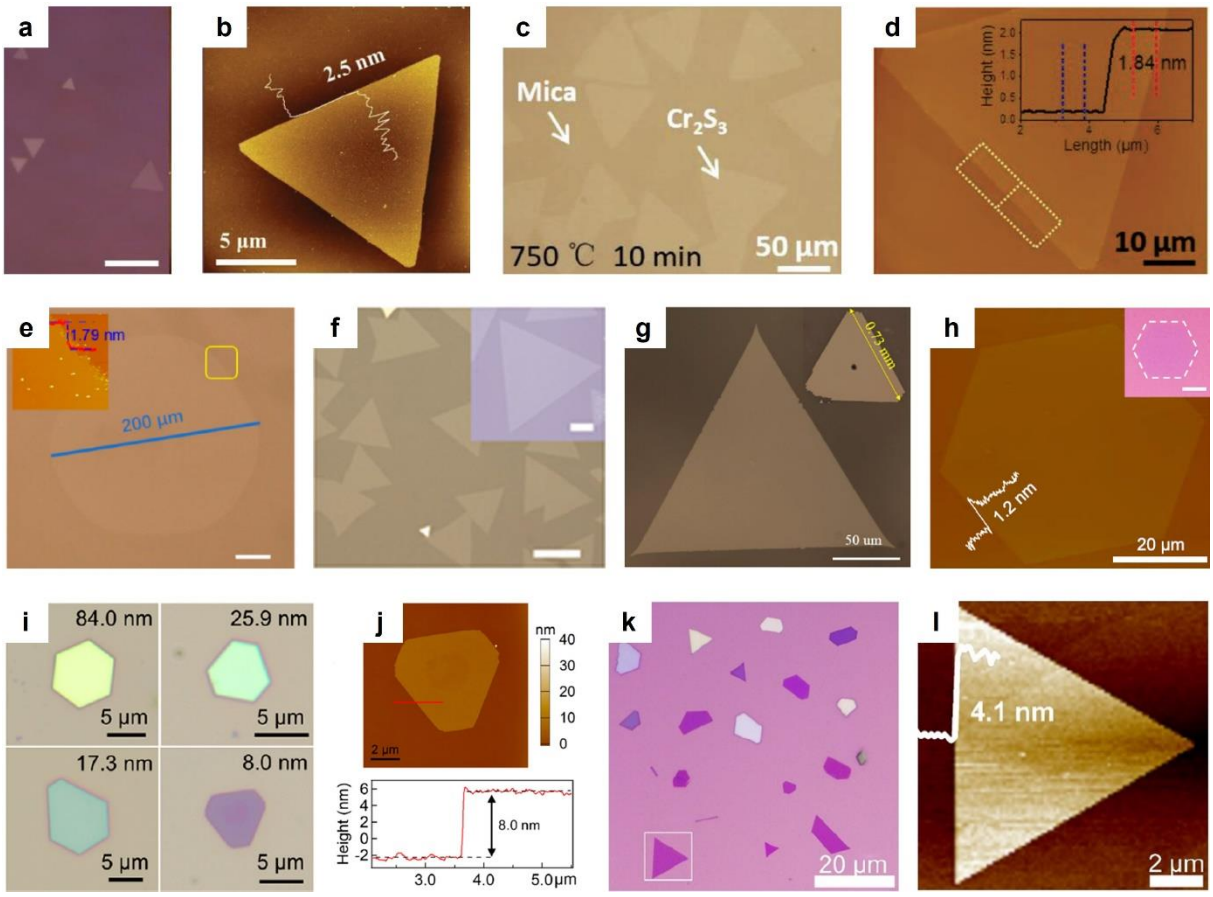

Figure 4. (a-b) The optical and AFM images of the CVD-grown Cr_2S_3 with $CrCl_2$ serving as the metal precursor. Reproduced with permission from ref 55. Copyright 2018, Wiley-VCH.[55] (c-d) The optical and corresponding AFM images of the CVD-grown Cr_2S_3 with the mixture of Cr and NaCl serving as the metal precursor. Reproduced with permission from ref 41. Copyright 2019, Wiley-VCH.[41] (e-g) Optical images of the large-sized 2D Cr_2S_3, CrSe, and Cr_2Te_3 single crystals grown on mica substrates. Reproduced with permission from ref 50, 52, and 57, respectively. Copyright 2019, American Chemical Society.[50] Copyright 2019, Wiley-VCH.[52] Copyright 2020, American Chemical Society. [57] (h) AFM image and the corresponding optical image (inset) of the ultrathin $CrTe_2$ grown on SiO_2/Si substrate. Reproduced with permission from ref 51. Copyright 2021, Springer Nature.[51] (i) Optical images of the Cr_2Te_3 with various thicknesses grown on SiO_2/Si substrate. (j) AFM image of the 8 nm thick Cr_2Te_3 flake. Reproduced with permission from ref 56. Copyright 2020, American Chemical Society. [56] (k-l) Optical and corresponding AFM images of the ultrathin $CrSe_2$ flakes grown on SiO_2/Si

substrate. Reproduced with permission from ref 40. Copyright 2021, Springer Nature.[40] Scale bar: (a) 20 μm; (e) 5 μm; (f) 25 μm.

3.1.2 Choice of Substrate

As demonstrated in Table 1, fluorophlogopite ($[KMg_3(AlSi_3O_{10})F_2]$) mica and SiO_2/Si are the most commonly used substrates for the growth of 2D Cr_mX_n. Mica is an atomically flat and dangling bond-free substrate with a lower migration barrier, which facilitates the attachment of precursors onto the edge of samples, promoting the horizontal rather than vertical growth of samples.[88-90] Notably, the preparation of large-sized 2D Cr_2S_3, CrSe, and Cr_2Te_3 single crystals on mica substrates with lateral sizes up to 200 μm have been achieved by Chu et al.,[50] Zhang et al.,[52] and Wen et al.,[57] respectively (Figure 4e-g). Zhou et al. have investigated the effect of different substrates on Cr_2S_3 growth and found that compared to mica, flakes grown on SiO_2/Si substrate exhibit worse morphologies.[55] This should stem from the fact that SiO_2/Si has much more dangling bonds on the surface.[91, 92] Nevertheless, researchers have never stopped the exploration of optimal synthesis conditions of 2D Cr_mX_n on SiO_2/Si.

Unlike the material grown on mica, where sample transfer and annealing processes are generally required for subsequent characterizations and electronic applications, Cr_mX_n grown on SiO_2/Si can be used directly for further studies, which is more efficient in revealing and applying their intrinsic properties. In 2020, Coughlin et al. attempted the direct growth of Cr_2Te_3 on SiO_2/Si substrate, and the smallest sample thickness they have achieved is around 8 nm, as shown in Figure 4i-j.[56] Another attempt has also been made by Li et al. for the growth of $CrSe_2$, and thinner flakes around 4.1 nm on SiO_2/Si have been obtained (Figure 4k-l).[40] Recently, the direct growth of ultrathin $CrTe_2$ on SiO_2/Si around 1.2 nm has been demonstrated by Meng and co-workers, as displayed in Figure 4h.[51] However, the synthesis depends sensitively on the growth atmosphere such as temperature and carrier gas, in other words, a

slight change in the environment may affect the sample formation and thickness significantly, which will be discussed in the later parts. Very recently, we have also demonstrated the successful synthesis of 2D Cr_5Te_8 on SiO_2/Si substrate.[53] The grown materials together with the SiO_2/Si substrate were used directly for the fabrication of Hall bar devices.

3.1.3 Growth Temperature

Temperature plays an essential role in the CVD synthesis of 2D TMCs. A subtle temperature change may lead to a substantial change in the final product, as the saturation pressure of the gasified precursors, the reaction rate of reactants, and the deposition rate of products will all be affected.[21, 93, 94] Recent studies have also revealed the significant effect of temperature on the CVD-grown Cr_mX_n, including sample thickness, lateral size, and phase structure.

According to the study reported by Meng et al., the thickness of the CVD-grown $CrTe_2$ sample is very sensitive to growth temperature.[51] A slight increase of the temperature from 973 K to 993 K can lead to a vast increase in the sample thickness from about 1.2 nm to about 47.9 nm, as shown in Figure 5a. The strong positive correlation between thickness and growth temperature was also discovered in many other Cr_mX_n, such as Cr_2S_3, Cr_5Te_8, and $CrSe_2$ (Figure 5b-d),[40, 41, 58] providing a direction for the precise thickness control of the 2D sample. Generally, thermodynamics will dominate the growth at a higher temperature, thereby resulting in the formation of a thicker sample with lower overall surface energy. In contrast, growth at a lower temperature is more dictated by edge energetics. Chemical precursors tend to be added to the fastest-growing front at the edges of the 2D nanosheets to expand the 2D crystal in the lateral dimension.[40, 95, 96]

It is noted that even though increasing the temperature will lead to the formation of unwanted thicker samples, larger-sized flakes will generally be resulted, which is more desirable in this regard. As demonstrated in Figures 5b and c, the lateral size of Cr_5Te_8 and Cr_2S_3 are found to

increase as the growth temperature increases. A higher growth temperature can promote the surface migration of precursors and the crystallization of Cr_mX_n flakes. However, over high temperature will lead to desorption and destruction of the growth front, thereby resulting in smaller sample size, as reported by Chu et al. (Figure 5e).[57]

Apart from the well-studied effect on thickness and size, temperature was found to possess a prominent effect on phase structure as well. Recently, we have demonstrated that the intriguing Cr_5Te_8 sample in both trigonal and monoclinic phases can be selectively synthesized by tuning the growth temperature.[53] As shown in Figure 5f, the thermodynamically more favorable trigonal Cr_5Te_8 can be obtained at a higher temperature, whereas the structurally more distorted monoclinic phase is preferably grown at a lower temperature. Finding the optimal temperature is thus of great importance in guaranteeing the achievement of phase-controlled synthesis of 2D Cr_mX_n with a large domain size.

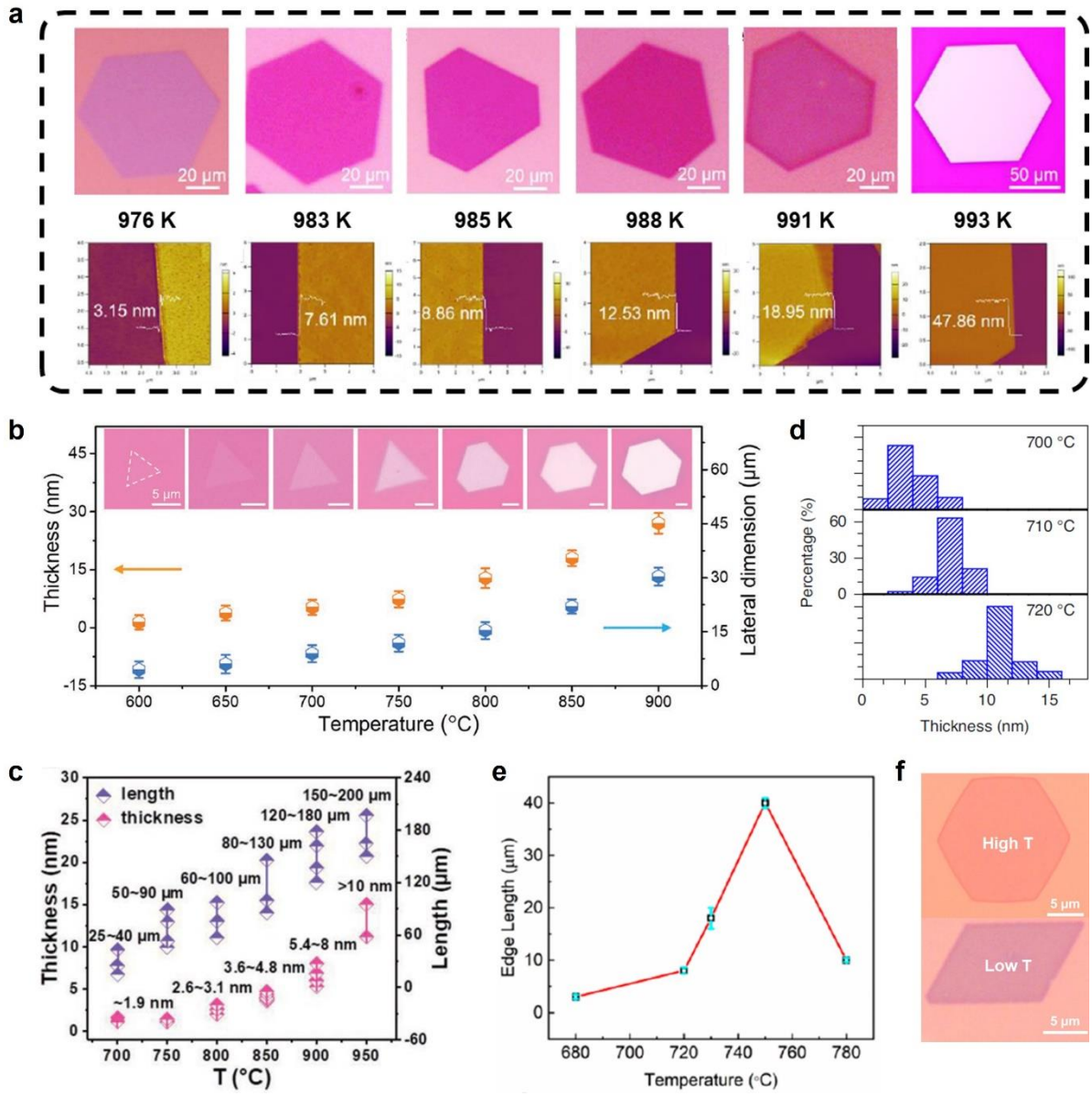

Figure 5. (a) Optical and corresponding AFM images of CVD-grown $CrTe_2$ flakes obtained at different temperatures displaying various thicknesses. Reproduced with permission from ref 51. Copyright 2021, Springer Nature.[51] (b) Temperature-dependent thickness and lateral dimension evolutions of CVD-grown Cr_5Te_8 flakes. Inset presents the corresponding optical images. Reproduced with permission from ref 58. Copyright 2021. Wiley-VCH.[58] (c) Statistical analysis of the thickness and lateral size of the CVD-grown Cr_2S_3 flakes synthesized at different temperatures. Reproduced with permission from ref 41. Copyright 2019. Wiley-VCH.[41] (d) Temperature-dependent thickness distribution of the CVD-grown $CrSe_2$ nanosheets. Reproduced with permission from ref 40. Copyright 2021, Springer Nature.[40] (e) Temperature-dependent edge size evolution of CVD-grown Cr_2S_3. Reproduced with permission from ref 50. Copyright 2019, American Chemical Society.[50] (f) Optical images of trigonal and monoclinic Cr_5Te_8 synthesized at different temperatures. Reproduced with permission from ref 53. Copyright 2022, Springer Nature.[53]

3.1.4 Deposition Time

Apart from the growth temperature, deposition time is found to be another important factor affecting the morphology of the grown Cr_mX_n flakes. Chu et al. demonstrated that larger Cr_2S_3 flakes could be obtained with prolonged growth time.[50] Representative OM images of Cr_2S_3 grown at different lengths of time are presented in Figure 6a, exhibiting the noticeable size change of the CrSe domains. Similar findings were also reported in CVD-grown CrSe, in which the highly linear correlation between CrSe flake size and deposition time was revealed (Figure 6b).[52] Notably, continuous Cr_mX_n film may also be obtained by proper tuning of the deposition time, as evidenced by the recent report of Cr_5Te_8 film which was obtained on the mica substrate upon extending the growth time from 10 to 30 min (Figure 6c).[58]

Apart from the change of flake size, shape transition may also be induced under sufficiently long deposition time due to the varied chalcogen to chromium (X : Cr) ratio. For instance, Chu and co-workers have reported the abnormal shape transition of Cr_2S_3 flakes from triangular to hexagonal shape, which is observed beyond the growth time of 30 min (Figure 6d).[50] The increased S:Cr ratio during the growth process results in the faster growth of Cr-terminated edges than S-terminated edges, thereby leading to the formation of truncated triangular shapes.

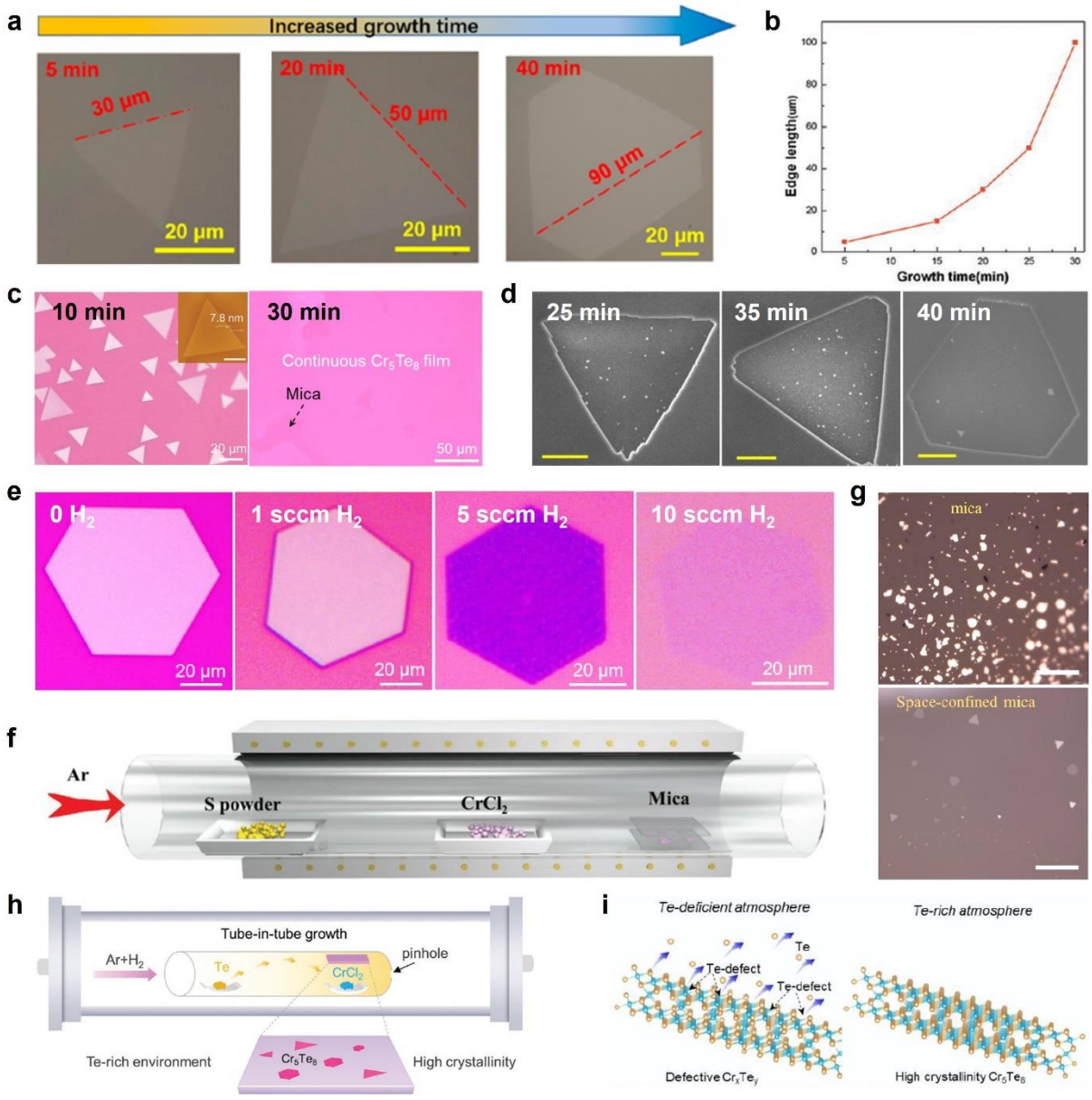

Figure 6. (a) Optical images of CVD-grown Cr_2S_3 nanoflakes obtained at different growth times. Reproduced with permission from ref 50. Copyright 2019, American Chemical Society.[50] (b) Growth time-dependent size evolution of CrSe nanosheets. Reproduced with permission from ref 52. Copyright 2019. Wiley-VCH.[52] (c) Optical images of 2D Cr_5Te_8 grown for different lengths of time. Reproduced with permission from ref 58. Copyright 2021. Wiley-VCH.[58] (d) Scanning electron microscopy (SEM) images of Cr_2S_3 nanosheets revealing time-dependent shape evolution. Scale bar: 20 μm. Reproduced with permission from ref 50. Copyright 2019, American Chemical Society.[50] (e) Optical images of $CrTe_2$ grown at different H_2 gas flow rates. Reproduced with permission from ref 51. Copyright 2021, Springer Nature.[51] (f) Schematic illustration of the space-confined CVD setup for the synthesis of Cr_2S_3. (g) Optical images of Cr_2S_3 flakes grown with (bottom) and without (top) space-confined method on mica. Scale bar: 20 μm. Reproduced with permission from ref 55. Copyright 2018, Wiley-VCH.[55] (h) Schematic illustration of the tube-in-tube CVD setup for the synthesis of Cr_5Te_8

nanosheets. (i) Schematic diagram of the formation of defective and high crystallinity Cr_5Te_8 under Te-deficient and Te-rich atmosphere, respectively. Reproduced with permission from ref 58. Copyright 2021, Wiley-VCH.[58]

3.1.5 Carrier Gas

In addition to the commonly used Ar gas, which transports the evaporated chalcogen precursors to the reaction zone, H_2 gas also plays an indispensable role in the synthesis of Cr_mX_n, as summarized in Table 1. The introduction of H_2 can generate the more reductive hydrogen chalcogenides (i.e., H_2S, H_2Se, and H_2Te),[97, 98] which is conducive to the reaction with Cr precursors, thereby leading to the formation of Cr_mX_n. Moreover, Meng et al. showed that within a certain range, increasing the H_2 concentration can also reduce the sample thickness, which is known as the etching effect.[51] Figure 6e presents OM images of $CrTe_2$ grown under different H_2 concentrations, clearly demonstrating the reduced thickness with increased H_2 concentration, which is of great value for the preparation of ultrathin Cr_mX_n layers.

3.1.6 CVD Setup

Apart from the aforementioned synthesis parameters, researchers have also made a great effort in designing the CVD setup in order to achieve the controllable synthesis of Cr_mX_n. As described above, most Cr_mX_n are non-van der Waals materials and thermodynamically stable in the form of 3D bonding. To obtain ultrathin 2D non-van der Waals materials, the thermodynamic growth should be suppressed, and growth should be governed by kinetics.[99] To solve this issue, a confined-space strategy was proposed by Zhou et al. in 2018 (Figure 6f).[55] A local environment is constructed in the inner space of the mica-sandwich configuration, where the concentration of precursors is remarkably lowered and thus the growth speed of materials is suppressed. A direct comparison between the confined-space and conventional

CVD methods has been made and demonstrated in Figure 6g. From which the positive effect of confined space on the growth of ultrathin samples is evidenced.

In an effort to achieve the controlled growth of Cr_mTe_n with accurate compositions, Chen and colleagues introduced a tune-in-tube growth approach, as illustrated in Figure 6h.[58] A built-in quartz tube with one side open and the other side semi-open was put inside a tube furnace to serve as the reaction system. This approach can provide a Te-rich environment throughout the growth process, which is conducive to suppressing the equilibrium shift toward the decomposition direction and favoring the shift toward the synthesis reaction direction (Figure 6i).

3.2 CVD-Grown Iron Chalcogenides (Fe_mX_n)

3.2.1 CVD Setup

CVD methods used to synthesize 2D iron chalcogenides are summarized in Table 1. The experimental setting for a typical CVD process is shown in Figure 7a.[39] Iron chlorides with relatively controllable vapor pressure were usually used as the iron source and placed at the center of the tube furnace. Se or Te powders were used as chalcogenide sources and placed upstream. A mixture of Ar and H_2 was selected as the carrier gas. Further, by playing with reaction temperature, flow, and substrate, one can prepare 2D iron chalcogenides with controlled phase, thickness, and composition.

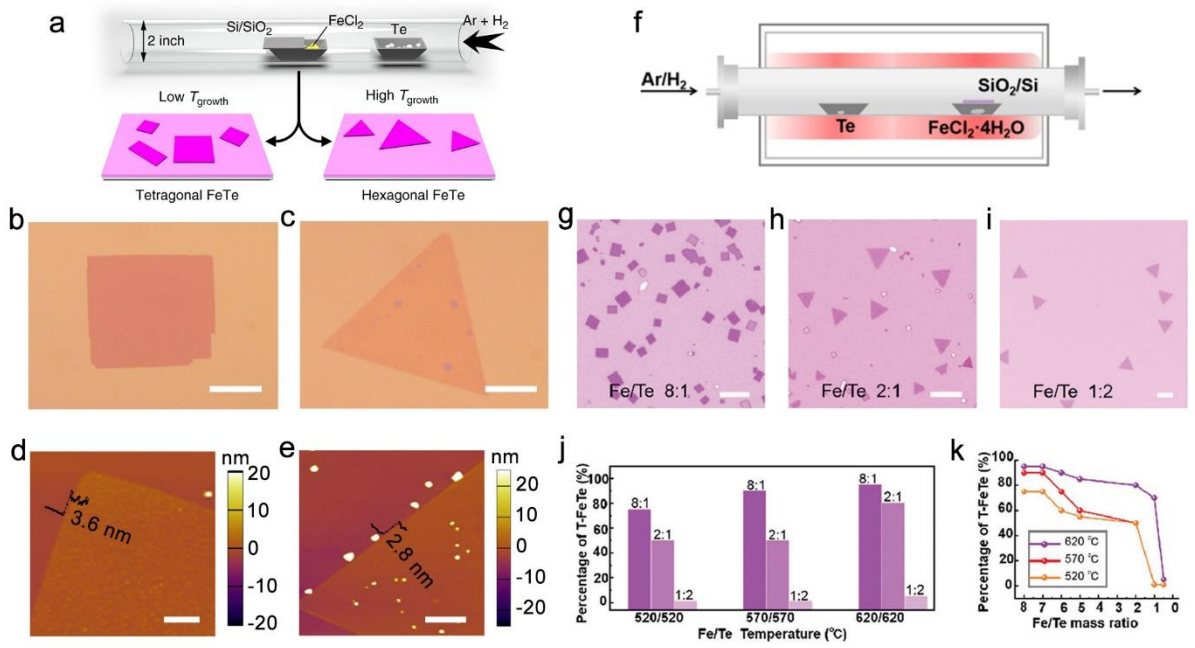

Figure 7. (a-e) Model demonstrating the controlled synthesis of two phases of FeTe by controlling the reaction temperature and the corresponding optical images and AFM results: (b, d) tetragonal FeTe and (c, e) hexagonal FeTe, respectively. Reproduced with permission from ref 39. Copyright 2020, Springer Nature.[39] (f) Experimental setting of controlling the phase of FeTe by precisely controlling the temperature of Fe and Te sources respectively and (g-k) the corresponding results. (g-i) The optical images of the products when the mass ratio of Fe and Te sources change from (g) 8:1, (h) 2:1 to (i) 1:2, respectively, while keeping the temperatures of both the Fe and Te sources to be 520 °C. (j) Relation between the percentage of tetragonal FeTe products to the Fe/Te temperature and Fe/Te mass ratio. (k) Percentage of tetragonal FeTe under different Fe/Te mass ratios keeping two-zone temperatures to be 620, 570, and 520 °C. Reproduced with permission from ref 75. Copyright 2021, Wiley-VCH.[75] Scale bar: (b, c) 20 μm; (d) 2 μm; (e) 3 μm; (g-i) 10 μm.

3.2.2 Phase Controlled Synthesis

The complicated phase diagram of iron chalcogenides makes it challenging to synthesize the controlled phase, which is also a platform for us to practice the CVD technique and gain knowledge about how the chosen parameters would influence the products. Several works were dedicated to controllably growing tetragonal and hexagonal FeTe phases recently.[39, 67] The two phases of FeTe have different magnetic properties. In addition, the doping of tetragonal FeTe

can result in a superconducting phase. One can expect to study the interplay between different magnetic phases and superconductivity if the controllable synthesis of the desired phase of FeTe can be realized. The first work reported that the CVD synthesis of different FeTe phases could be controlled by controlling the reaction temperature, as shown in Figure 7a-e.[39] It turns out that the lower synthesis temperature favors the formation of the tetragonal phase, while the higher synthesis temperature favors the formation of the hexagonal phase (Figure 7b-c). At the middle-temperature window, the coexistence of hexagonal and tetragonal phases can be found. This can be explained by the difference in thermodynamic energy of the two phases.[61, 62, 64, 100, 101] This trend is also consistent with another work published by Wang et al. despite the difference in the reaction temperature, which could be due to the different experimental settings.[73] In this work, the author found the existence of the superlattice structure. Also, the prepared tetragonal FeTe nanosheets show the superconducting feature, which was explained by oxygen doping. These results show that the CVD-prepared samples can show different properties from their bulk materials, and there is still plenty of room for exploration. In another work, the selective growth of different FeTe phases was further studied by controlling the heating temperature of iron precursors and Te precursors separately (Figure 7f-k).[75] The results show that the ratio between the Fe and Te precursors is the key parameter in determining the phase of the products. With a decrease in the Fe/Te precursor mass ratio ranging from 8:1 to 1:2, the dominant phase in the products changes from tetragonal phase to hexagonal phase while keeping the reaction temperature the same, as shown in Figure 7g-i. By this method, the hexagonal FeTe, which was claimed to be prepared at a temperature over 570 °C in the abovementioned work, can be prepared at a much lower reaction temperature. This work reveals the key parameter in the selective synthesis of FeTe nanocrystals by the CVD method, which enriches our understanding of the fundamental CVD process to control the phase.

3.2.3 Choice of Substrate

The previous study on CVD shows that the substrate plays a significant role in the growth of 2D materials. The commonly used substrate is SiO_2/Si owing to its compatibility with Complementary metal-oxide-semiconductor (CMOS) technology. Besides SiO_2/Si, mica can also be an essential substrate for the growth of 2D materials. Unlike the amorphous surface of SiO_2/Si, the layered mica can facilitate the growth by van der Waals epitaxy. Non-layered 2D iron chalcogenide, such as Fe_7Se_8, can only be grown on the mica substrate (Figure 8a-d). The prepared 2D Fe_7Se_8 can be as thin as 3.5 nm, showing thickness-dependent magnetism.[42] This method provides a platform to study magnetism in 2D non-layered materials. Besides, the use of mica as a growth substrate can also have other advantages. In another work, Liu et al. reported the synthesis of $FeSe_2$ nanocrystals on mica substrate (Figure 8e-g).[72] The size of the prepared nanocrystal can be over 100 μm, which makes it easy to pattern electrodes on the sample and study electrical properties on the single nanocrystal level. Shi et al. also reported the growth of 2D magnetic FeTe nanocrystals on mica substrate.[70] The prepared sample can be as thin as 2.3 nm and as large as 120 μm. The hexagonal products show ferromagnetism with the Curie temperature near 300 K. Further, the author developed a PS-assisted method to transfer the prepared FeTe nanocrystals from mica to other substrates by making use of the hydrophilic nature of mica (Figure 8h). The transferred products exhibit good quality, as confirmed by STEM and transport data. These results show that it is possible to synthesize novel iron chalcogenides nanocrystals by discovering suitable growth substrates.

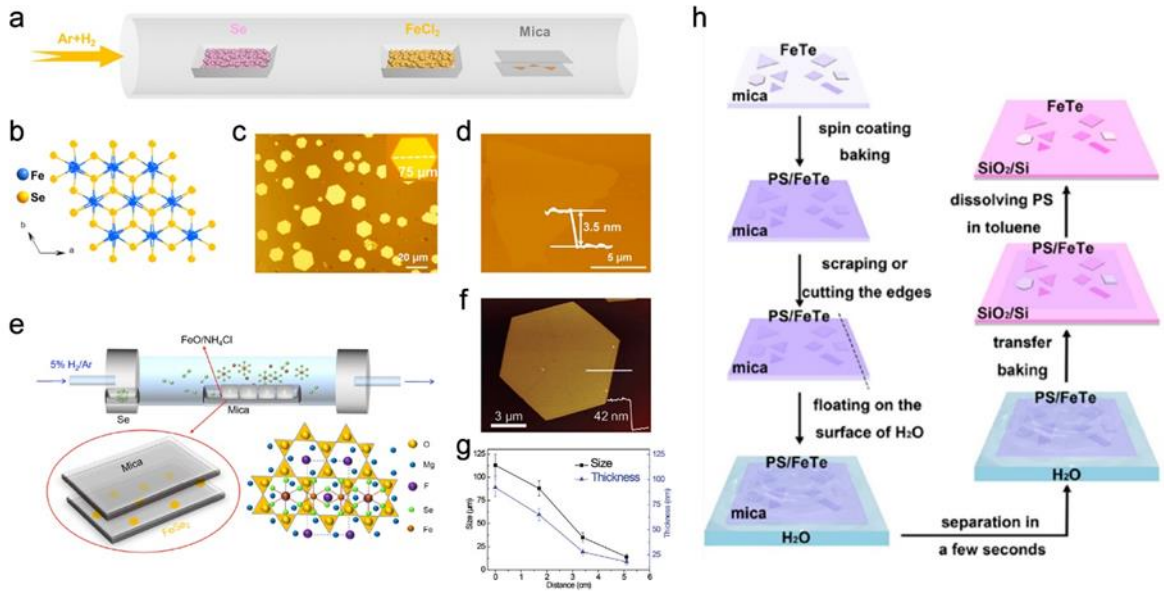

Figure 8. (a-d) CVD synthesis of Fe_7Se_8 nanoflakes on mica substrates: (a) Experimental setting, (b) Top view of the crystal structure of Fe_7Se_8, (c) Optical images of Fe_7Se_8 nanoflakes, and (d) the corresponding AFM results and height profile. Reproduced with permission from ref 42. Copyright 2022, American Chemical Society.[42] (e-g) CVD synthesis of $FeSe_2$ nanoflakes on mica substrates: (e) Experimental setting, (f) AFM surface topography and height profile of a hexagonal shape $FeSe_2$ nanocrystal with a thickness of 42 nm, and (g) Results showing the dependence of sizes and thicknesses of the products on the distance between mica and the Fe source. Reproduced with permission from ref 72. Copyright 2021, Wiley-VCH.[72] (h) The processes of transferring $FeTe_2$ nanoflakes from mica to SiO_2/Si substrate. Reproduced with permission from ref 70. Copyright 2021, American Chemical Society.[70]

3.2.4 Synthesis of Ternary Compounds

Besides the binary compounds, the CVD method can also be used to prepare the ternary iron chalcogenides. Magnetic Fe_xGeTe_2 nanocrystals were prepared by a salt-assisted CVD method.[74] The products show clear reflective magnetic circular dichroism (RMCD) signals demonstrating the existence of ferromagnetism and have a curie temperature close to room temperature. The use of salt might be the key to successfully synthesizing this ternary magnetic material. The main challenge in CVD synthesizing ternary compounds is that there would be phase segregation. This pioneering work demonstrates the possibility of synthesizing 2D

ternary magnetic materials by the CVD method. Further exploration for controlling their phase purity and synthesizing other ternary magnetic materials is worth trying.

3.3 Other CVD-Grown TMCs

Apart from chromium and iron, vanadium and manganese are also elements often related to magnetism. Preparation of 2D vanadium chalcogenides (V_mX_n), including V_5S_8, VS_2, VSe_2, and VTe_2, has also been achieved with the CVD method.[37, 44, 45, 102-104] In a typical CVD synthesis procedure, VCl_3 was usually selected as the vanadium precursor and placed at the upper stream of the growth substrate. Chalcogenide powders were heated at a lower temperature and turned to the liquid state during the reaction. The CVD method is very similar to that used to prepare chromium and iron chalcogenides. When SiO_2/Si substrate was used as the growth substrate, single-crystalline vanadium chalcogenide nanosheets can be prepared, whose lateral sizes can be as large as 10 μm. For V_5S_8 and VSe_2, ultrathin nanosheets with several layers can be obtained (Figure 9a, e).[44, 45] Thus, the thickness-dependent electrical properties of the vanadium chalcogenides can be studied by patterning electrodes on a single-crystalline nanosheet.

Interestingly, unusual magnetic behaviors in the CVD synthesized V_mX_n were reported in several works. For example, the thickness-dependent anomalous Hall effect was discovered in V_5S_8 nanosheets prepared by the CVD method (Figure 9c-d).[44] V_5S_8 is an intrinsic antiferromagnetic metal. However, when its thickness decreases, the magnetic order changes to a spin-glass-like state at first and becomes weak ferromagnetism when thickness further decreases below 3.2 nm. The result shows a competition between the antiferromagnetic and ferromagnetic phases when the thickness of V_5S_8 decreases, which can be understood as the balance between the alternating spin layers was changed (Figure 9b). In another work, the CVD

approach was also used to prepare single-crystalline VSe_2 nanosheets.[45] Thickness-dependent magnetotransport behaviors were also observed in the transport measurements. An obvious CDW transition peak was observed in the temperature dependence of resistivity (ρ-T) curve of VSe_2 nanosheets when its thickness is larger than 6 nm, showing a 3D transport characteristic. When the sample thickness becomes lower, the quantum confinement starts to take effect and makes the band structure of VSe_2 transit to a quasi-2D one, which gives rise to the weak antilocalization by largely increasing the phase coherence length even though the spin-orbit coupling of VSe_2 is challenging to be observed due to the small atomic numbers of V and Se (Figure 9f). By the same method, VTe_2 nanocrystals with lateral sizes up to 10 μm can also be prepared by the CVD method (Figure 9g).[103] Interestingly, the Kondo effect was discovered in the cryogenic transport study (Figure 9h), which is believed to originate from the existence of interstitial vanadium ions by DFT calculations. These results show that the CVD synthesized vanadium chalcogenides can be a platform to study the physics of the magnetic properties, strong correlation, and many-body effect.

In the case of manganese, manganese chalcogenides (M_mX_n) are not layered materials. However, using mica as the growth substrate, ultrathin M_mX_n can be prepared, including MnS, MnSe, and MnTe (Figure 9i).[46, 105, 106] This makes it possible to study their transport properties on single-crystalline nanomaterials. In a recent work published by Li et al.,[46] the transition from antiferromagnetism to paramagnetism of CVD synthesized α-MnTe nanosheets were characterized by magnetotransport, and the competition between thermally excited magnons and lattice phonons was observed (Figure 9j). All the above demonstrates that CVD is a powerful technique to prepare 2D magnetic TMCs, and more fascinating phenomena in other compounds and their heterostructures are awaiting exploration.

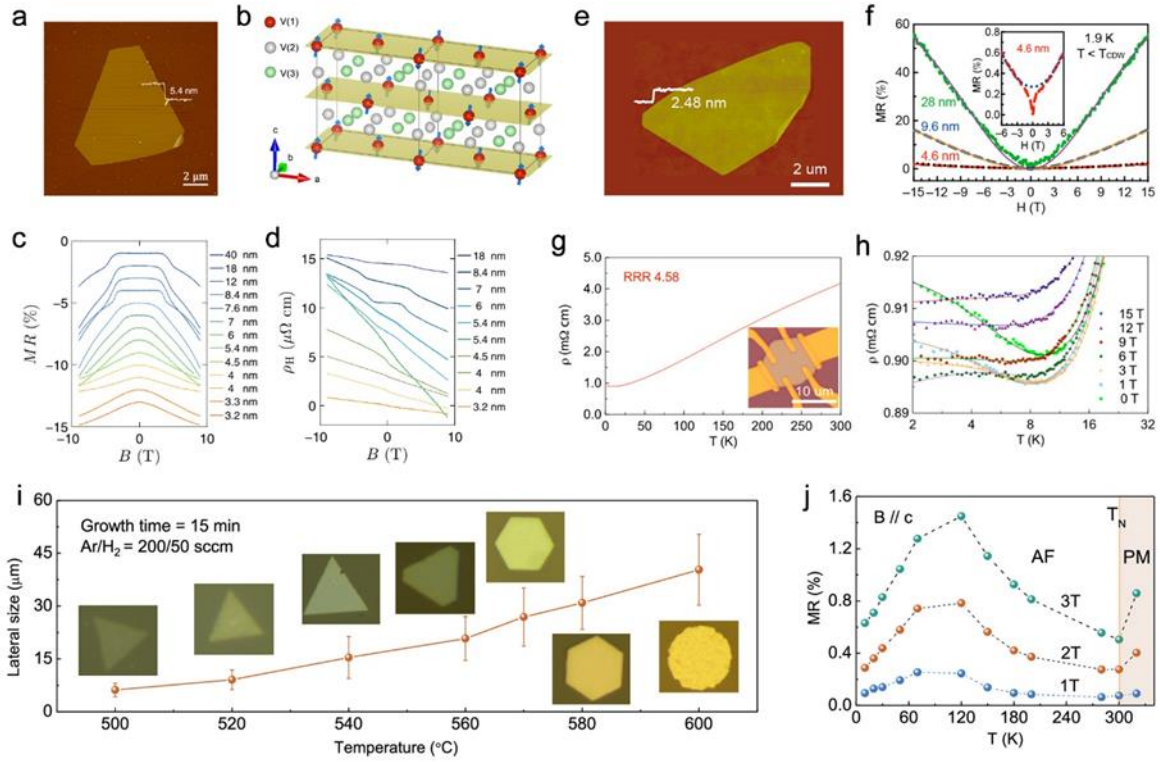

Figure 9. (a-d) AFM image, atomic structure, and magnetic properties of CVD synthesized V_5S_8 nanocrystals: (a) AFM image of a 5.4-nm V_5S_8 nanosheet; (b) Atomic and spin structures of V_5S_8; (c) Thickness-dependent longitudinal magnetoresistance and (d) Hall resistivity. Reproduced with permission from ref 44. Copyright 2017, American Physical Society.[44] (e) AFM image and (f) magnetoresistance of the CVD synthesized VSe_2 nanosheet. Reproduced with permission from ref 45. Copyright 2019, American Chemical Society.[45] (g) Temperature-dependent resistivity (ρ−T) of a CVD synthesized VTe_2 nanosheet (inset is the optical image) and (h) the existence of resistivity upturn at low temperature. Reproduced with permission from ref 103. Copyright 2019, American Chemical Society.[103] (i) Evolution of the products of CVD synthesized MnTe nanosheets and (j) their transition from antiferromagnetism to paramagnetism characterized by magnetoresistance. Reproduced with permission from ref 46. Copyright 2022, American Chemical Society.[46]

4. Physical properties of 2D magnetic TMCs

4.1 Magnetic Properties

Owing to the half-filled 3d band, chromium and iron are frequently related to magnetism. Bulk chromium and iron-based chalcogenides crystals have attracted extensive research interest due

to their robust magnetic ordering.[63, 65, 107-109] A variety of magnetic behaviors, such as ferrimagnetism,[110, 111] ferromagnetism,[63, 108] and antiferromagnetism[64, 112] were proven to be present in Cr_mX_n and Fe_mX_n compounds by varying the chalcogen elements. With the reduction of dimensionality, 2D Cr_mX_n and Fe_mX_n crystals show very peculiar magnetic properties and often bring about layer-dependent magnetism due to the size effects.[51, 53, 56] 2D Cr- and Fe-chalcogenides can also offer tunable structural phases with distinct magnetic properties.[39, 53] In this section, the magnetic anisotropy together with thickness and phase-dependent magnetic properties of 2D magnetic Cr_mX_n and Fe_mX_n will be summarized and discussed.

4.1.1 Magnetic Anisotropy

Magnetic anisotropy is the property that confers a preferred direction on the spin or magnetic moment of a system that may not be aligned with an external magnetic field, which plays a vital role in various static and dynamic properties of magnetic materials. In particular, magnetic anisotropy is an essential prerequisite for avoiding thermal fluctuation induced random spin reorientation and stabilizing the ferromagnetic order in the 2D limit. Bulk CrTe crystals were proven to be ferromagnetic with strong perpendicular magnetic anisotropy,[113] which implies that ultrathin CrTe may maintain its ferromagnetic properties even when the thickness decreases to the nanometre scale. Through MOKE measurements, Wang et al. demonstrated that the hard magnetism with strong out-of-plane ferromagnetic anisotropy sustains quite well in CVD synthesized CrTe flakes as the thickness varies from 45 nm to 11 nm.[54] The perpendicular magnetic anisotropy was also discovered in many other chromium and iron-based chalcogenides, such as Cr_2Te_3,[56, 57] Cr_5Te_8,[53] $CrSe_2$,[40] Fe_7Se_8[114], and hexagonal FeTe,[39] which offers superior qualities for these 2D magnetic TMCs in high density, fast access, and low power memory devices. In contrast, in-plane magnetic anisotropy has rarely been reported in CVD synthesized 2D Cr_mX_n and Fe_mX_n except for Cr_2S_3.[41, 50] Interestingly, the magnetic

anisotropy of 1T-$CrTe_2$ was found to be transformed from in-plane to out-of-plane with the decrease of thickness from 40 to 3 nm and the critical thickness was observed to be ~ 10 nm.[51] This anomalous thickness-dependent phenomenon is attributed to the electrostatic coupling between the sample and the substrate. The Coulomb screening is weakened in the atomic 2D $CrTe_2$ compared to the 3D bulk crystal, resulting in a large on-site Coulomb potential from the electrostatic interaction with the substrate, which might eventually flip the easy axis.[51]

4.1.2 Thickness Dependency

The thickness-dependent phenomenon becomes prominent when the dimension of the magnetic TMCs is decreased from 3D to 2D as a result of quantum confinement and the weakened Coulomb screening,[51] which can be utilized to tune the magnetic properties of the pristine layer. A typical example is the tunable Curie temperature (T_C) and coercivity field (H_C) along with the change of the layer number. Recent advances in the controllable CVD growth of thickness-tunable TMCs allow researchers to systematically explore the thickness-dependent magnetic properties. Li and co-workers used RMCD to investigate the magnetic phase diagram of few-layered $CrSe_2$ nanosheets with variable thicknesses grown on the WSe_2 substrate.[40] The RMCD measurements for $CrSe_2$ with different layer numbers at 15 K are shown in Figure 10a. From which clear hysteresis loops were observed in few-and multi-layered samples, indicating the ferromagnetic nature of the $CrSe_2$. Moreover, strong thickness-dependency was revealed, as evidenced by the increased coercivity along with the increase of the layer number (Figure 10b). The reported magnetic phase diagram in Figure 10c demonstrated that ferromagnetic ordering was maintained at the monolayer limit with a T_C of 65 K, and the T_C gradually increases with thickness, reaching 110 K (i.e., the bulk value) at the thickness of 16 or more layers.

Apart from $CrSe_2$, the positive correlation between the magnetic response and sample thickness

was also reported in many other ferromagnetic TMCs. For instance, the evolution of ferromagnetic properties of trigonal Cr_5Te_8 crystals from bulk to the 2D limit has been investigated by Chen et al.[58] Magneto-optic Kerr effect (MOKE) spectroscopy was adopted to probe the temperature-dependent magnetic response of Cr_5Te_8 with different thicknesses. Hard magnetic characteristics of Cr_5Te_8 down to 10 nm were revealed by the rectangular hysteresis loops measured at 50 K (Figure 10d). Similar to $CrSe_2$, T_C of CVD-grown trigonal Cr_5Te_8 also increases with increasing sample thickness, as shown in the magnetic phase diagram in Figure 10e. Recently, we have also studied the thickness effect on the ferromagnetic response of Cr_5Te_8 in both trigonal and monoclinic phases.[53] Apart from our experimental findings that T_C of bulk crystal is larger than that of thinner flakes for both monoclinic and trigonal Cr_5Te_8, we have further conducted DFT simulations. The T_C of Cr_5Te_8 in both bulk and flake form is estimated using mean-field approximation.[57] For both phases, T_C demonstrates a positive correlation with the sample thickness. This layer dependency is primarily determined by the renormalized surface spin states and surface-induced structural reconstruction, which are easily influenced by the thermal fluctuation due to the reduction of dimensionality.[14] Apart from Cr_mX_n, this normal T_C behavior is in line with most reported Fe-based ferromagnets. For example, the coercivity of Fe_7Se_8 was found to decrease with reducing the thickness, while the ferromagnetic ordering is preserved down to 7.8 nm (Figure 11a).[42] Moreover, transport results show that the magnetic orders of both tetragonal and hexagonal FeTe weaken with decreasing thickness (Figure 11c). As a result, the critical temperatures (i.e., Neel temperature and T_C) of the two phases decrease significantly when the thickness goes from 30 nm to several nanometers.[39]

Recently, there is an interesting phenomenon reported in the Cr_mX_n system, which is the anomalous thickness-dependent T_C, i.e., T_C increases as the sample thickness decreases. Wen et al. first reported this intriguing phenomenon in CVD-grown Cr_2Te_3.[57] When the thickness

of their Cr_2Te_3 samples was reduced from 40.3 nm to 5.5 nm, the T_C increased strongly from 160 K to 280 K (Figure 10f). As the authors pointed out, the mechanism of ferromagnetism in 2D Cr_2Te_3 is an open question, and the possible origin may be attributed to a doping mechanism or reconstruction of 2D Cr_2Te_3. A similar finding was also reported by Meng et al. in the study of CVD-grown $CrTe_2$ (Figure 10g).[51] They believed the anomalous thickness-dependent *Tc* should be attributed to the layer-dependent magnetic anisotropy. With reduced thickness, the Coulomb screening effect in thin films can change the easy axis to shift from in-plane to out-of-plane, giving rise to a lower *Tc* in the in-plane direction and higher *Tc* in the out-of-plane direction in atomically thin samples. However, it is worth mentioning that there are some discrepancies in the literature regarding the magnetic properties of the same respective compounds, i.e., Cr_2Te_3 and $CrTe_2$. [56, 115] Other research revealed an opposite thickness dependence, where the *Tc* decreases with decreasing thickness, contrary to the anomalous thickness dependence previously stated. The exhibited varying and sometimes even contrasting magnetic properties of 2D Cr_mTe_n should be due to the different intercalations of the Cr atoms in the van der Waals gap, as magnetism in Cr_mTe_n depends strongly on the composition and coordination environment.[84, 116-119] Therefore, it is imperative to correlate the magnetic phase with Cr-intercalation details to understand the intrinsic magnetism in this emerging 2D magnet family.

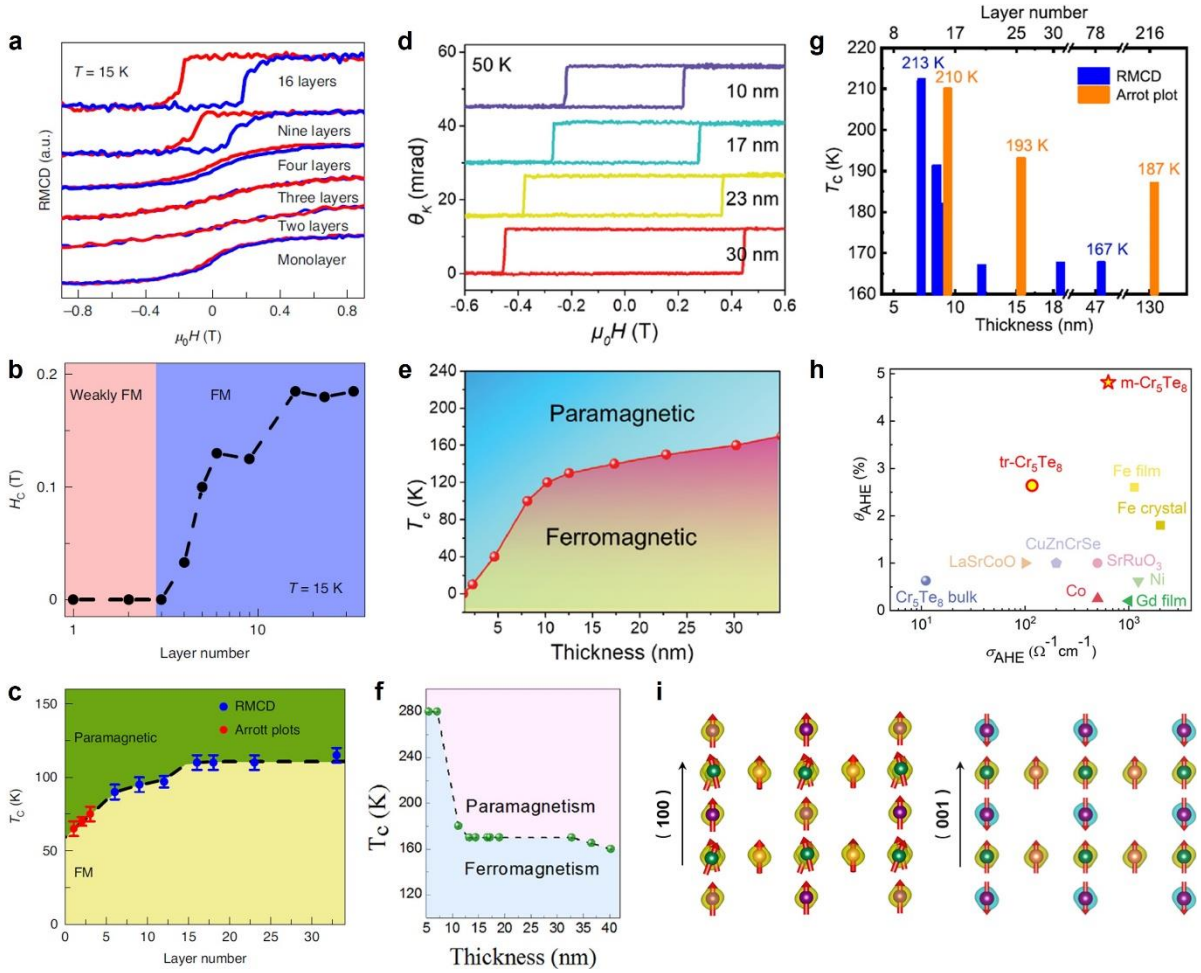

Figure 10. (a-c) Thickness-dependent magnetic properties of CVD-grown $CrSe_2$: (a) RMCD signals of 2D $CrSe_2$ nanosheets with different layer numbers measured at 15 K. (b) Layer-number-dependent H_C of $CrSe_2$ measured at 15 K. (c) Magnetic phase diagram of the CVD-grown $CrSe_2$. Reproduced with permission from ref 40. Copyright 2021, Springer Nature.[40] (d-e) Thickness-dependent magnetic properties of CVD-grown trigonal Cr_5Te_8: (d) MOKE signals of 2D Cr_5Te_8 nanosheets with different thicknesses measured at 50 K. (e) Magnetic phase diagram of the CVD-grown trigonal Cr_5Te_8. Reproduced with permission from ref 58. Copyright 2021. Wiley-VCH.[58] (f) Magnetic phase diagram of CVD-grown Cr_2Te_3 exhibiting anomalous thickness-dependent TC. Reproduced with permission from ref 57. Copyright 2020, American Chemical Society.[57] (g) T_C of CVD-grown $CrTe_2$ with varying thicknesses. Reproduced with permission from ref 51. Copyright 2021, Springer Nature.[51] (h) Phase-dependent anomalous Hall conductivity and anomalous Hall angle of trigonal and monoclinic Cr_5Te_8. (i) The spin ordering of m-Cr_5Te_8 (left) and tr-Cr_5Te_8 (right). Reproduced with permission from ref 53. Copyright 2022, Springer Nature.[53]

4.1.3 Phase Dependency

Cr_mX_n and Fe_mX_n possess a number of binary compounds and exhibit multiple structural phases with distinct physical properties. The alternating stacks of Cr-deficient and Cr-full layers along the c direction have been found to play an important role in determining the structural phase and magnetic properties of bulk Cr_mX_n.[118, 120] It is well known that the properties of 2D materials are dominated by their structures, and subtle structural changes could lead to very distinct properties.[121-123] Tuning the magnetic properties of 2D TMCs by manipulating their phase structures has thus attracted substantial research interest. Our recent work has revealed that compared to the conventional trigonal Cr_5Te_8, an enhanced anomalous Hall effect could be achieved in the more distorted monoclinic phase.[53] Specifically, monoclinic Cr_5Te_8 possesses higher T_C, larger conductivity, and Hall angle, as presented in Figure 9h. To gain more insight into the origin of the ferromagnetism in Cr_5Te_8 and the phase effect, DFT calculations were conducted and revealed that the spin-polarized states are originated from the d orbitals of Cr atoms (Figure 9i). Additionally, the monoclinic phase has much larger anisotropy than the trigonal phase, thereby leading to stronger magnetic stability, which was also supported by the Stoner criterion.

Apart from the magnetic chromium-based chalcogenides, rich magnetic orders also exist in iron chalcogenides. Taking FeTe as an example, tetragonal FeTe shows antiferromagnetism while hexagonal FeTe was reported to be ferromagnetic, which were both verified by the transport result (Figure 11b-d).[39] In this work, the origin of the ferromagnetism in the hexagonal FeTe is also explored by density-functional theory calculation. The result showed that a possible structural distortion could give a shorter interlayer Fe–Fe distance and enhance the FM direct exchange through the Fe-Fe bonding, which could be the origin of the observed ferromagnetism (Figure 11e-g).

It is worth mentioning that FeTe nanomaterials synthesized by different CVD methods were

reported to have different properties. The hexagonal FeTe was reported to be ferromagnetic by Cheng et al. and Kang et al.,[39, 69] whereas evidence of magnetism was not found by Wang et al.[67] One possible reason is that the magnetic properties of iron chalcogenides are very sensitive to defects. The slight difference in the synthesis condition could generate different kinds of defects. The doping of oxygen atoms in the CVD synthesized tetragonal FeTe was confirmed by Auger electron spectroscopy (AES) analysis and transport data (Figure 11g-j).[73] Considering that the iron precursors in these works are $FeCl_2$, which is very sensitive to moisture when exposed to the ambient condition, it is reasonable to assume that the hexagonal phase could also easily be contaminated by oxygen atoms. Besides, in layered materials, the strong correlation of intercalated ions can give rise to different magnetic orders.[76] The locally intercalated iron ions were unveiled by the STEM in two works.[73, 76] Considering that there is not an effective way to precisely control the amount of the intercalated iron ions, this is a possible reason that different magnetic properties were reported by different kinds of CVD methods.

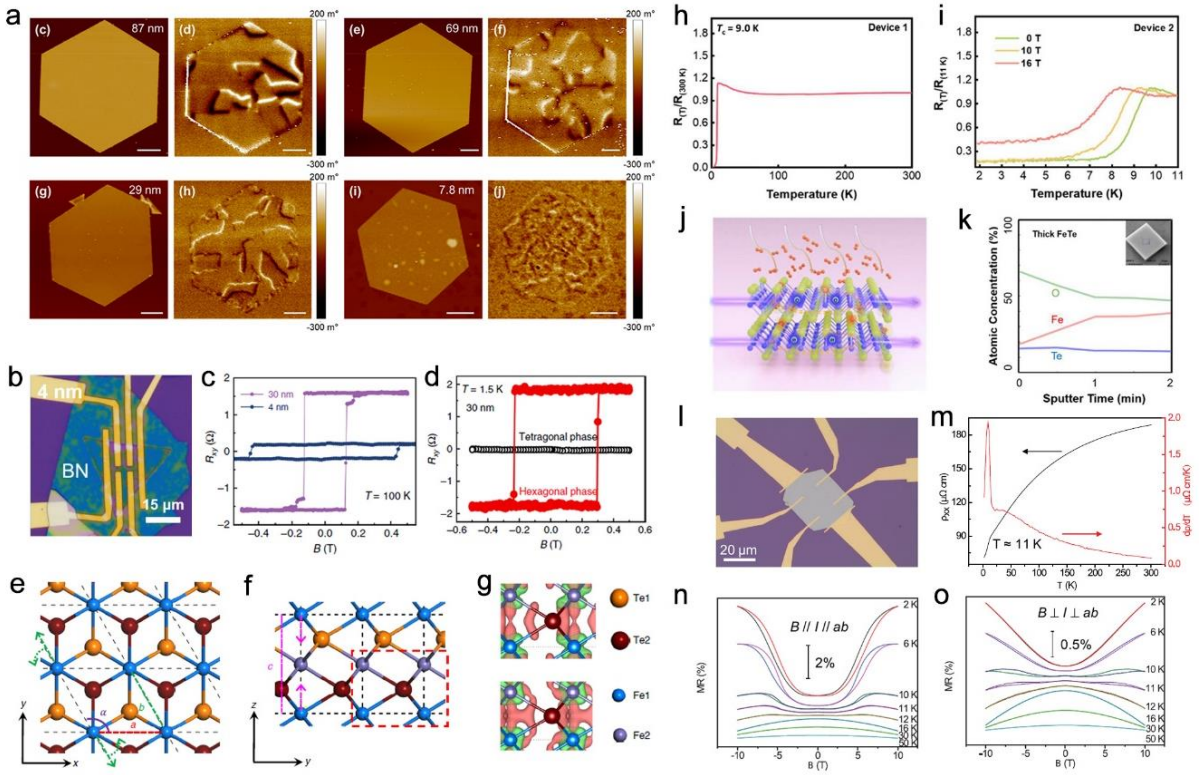

Figure 11. (a) Topography and corresponding MFM images of Fe_7Se_8 nanoflakes with different thicknesses. Reproduced with permission from ref 42. Copyright 2022, American Chemical Society.[42] (b-g) Magnetic properties of the CVD synthesized FeTe and theoretical calculation showing the origin of the magnetism: (b) Hall devices fabricated on a 4 nm hexagonal sample; (c) Anomalous Hall effect (AHE) hysteresis loops of hexagonal FeTe devices with 30 and 4 nm measured at 100 K; (d) The magnetic field dependence of the Hall resistance (R_{xy}) at 1.5 K corresponding to 32 nm tetragonal FeTe and 30 nm hexagonal FeTe; (e, f) Top view and Side view of distorted hexagonal FeTe; (g) Atomic differential charge densities of the undistorted and distorted structures in their most stable magnetic orders of the region marked in the red dashed rectangle in e. Reproduced with permission from ref 39. Copyright 2020, Springer Nature.[39] (h-k) Transport property and characterization of oxygen-doped tetragonal FeTe nanocrystals: (h) The temperature-dependent resistance; (i) The superconductivity transition temperatures under different magnetic fields; (j) Illustration of the tetragonal FeTe doped by O atoms, where red, yellow, and blue balls represent O, Te, and Fe atoms respectively; (k) Elemental depth analysis using AES of the superconducting sample. Scale bar: 2 μm. Reproduced with permission from ref 73. Copyright 2021, Elsevier.[73] (l-o) Low-temperature electrical transport properties of layered $FeSe_2$ nanocrystals: (l) Optical image of a Hall bar device patterned on a $FeSe_2$ nanocrystal, (m) Temperature-dependent resistivity of the layered $FeSe_2$ nanocrystal in l and its first derivative dρ/dT, and (n) Transverse and (o) longitudinal MRs dependence on magnetic fields at different temperatures. Reproduced with permission from ref 72. Copyright 2021, Wiley-VCH.[72]

4.1.4 Anomalous Magnetoresistance

Magnetoresistance (MR) is a characteristic that the resistance of a substance changes with an external magnetic field, which offers an efficient tool for probing the fundamental properties of the substance. This phenomenon has been well established for bulk Cr_mX_n and Fe_mX_n crystals such as $CrSe_2$,[124] $Cr_{0.92}Te$[125], and FeSe.[126] The versatile properties can be largely preserved in their 2D counterparts, and some distinctive characteristics can be introduced due to the quantum confinement effect. As for Fe_mX_n, besides the conventional magnetism in iron chalcogenides, an interesting anomalous magnetoresistance and phase transition in the CVD-grown $FeSe_2$ nanocrystals was reported.[72] The magnetoresistance exhibits a transition from negative to positive when cooling from 30 K to 2 K regardless of the direction of the magnetic field as shown in Figure 11l-o. The origin of this negative magnetoresistance was explained to

be magnetic field suppression scattering of spin fluctuations and competition of magnetic interactions induced by the phase transition.

4.2 Electronic Properties

The electronic properties of 2D magnetic TMCs are also of great importance for applications in electronic devices. Recently, an interesting thickness-dependent conduction type transition in 2D semiconducting Cr_2S_3 was reported by Cui et al.[41] By increasing the sample thickness, the conduction type could be effectively tuned from p-type to ambipolar, and then to n-type, as shown in Figure 12a-b. Moreover, the maximum hole mobility ($\approx 6.3 \times 10^{-3}$ cm^2 V^{-1} s^{-1}) and maximum electron mobility (≈ 1.8 cm^2 V^{-1} s^{-1}) were obtained for 3.6 nm and 12.5 nm thick Cr_2S_3 flakes, respectively, suggesting great electrical conductivity of 2D magnetic Cr_2S_3. As the authors discussed, the origin of the thickness-dependent conduction-type variation should be attributed to the fluctuation of the amount of Cr atoms in the alternating occupied $Cr_{1/3}$ atom planes with varying flake thicknesses. As thicker samples are generally obtained at a higher temperature, adequate Cr precursors can be evaporated and reacted, thereby providing excess Cr atoms in the $Cr_{1/3}$ planes. Excess Cr atoms behave as donors to induce n-type behavior of the thicker samples. In contrast, Cr vacancies behaving as acceptors would generally be introduced into the thinner samples due to the insufficient Cr supply at lower growth temperature and cause the p-type nature.

In recent years, the superconductivity in iron-based materials has also received enormous research attention.[127] The iron-based superconductors showed similar behaviors to cuprate superconductors, providing another platform to study unconventional superconductivity. Surprisingly, evidence of topological superconductivity was discovered in $FeTe_{1-x}Se_x$, characterized by angle-resolved photoemission spectroscopy (ARPES) and scanning tunneling

microscopy (STM) methods.[128, 129] Further results show that it is also possible to observe magnetism in this system.[130-133] The above results demonstrate that iron chalcogenides can be a platform to study the interplay of magnetism, topology, and superconductivity. In addition to the study on crystals, techniques for preparing their thin films are also attractive for future practical applications. Considering that it is challenging to mechanically exfoliate these iron-based superconductors due to their strong layer interaction, the CVD method is indeed an ideal choice. Recently, we reported an atmospheric CVD method to synthesize superconducting $FeTe_{1-x}Se_x$ nanosheets for the first time.[134] The lateral size of the prepared $FeTe_{1-x}Se_x$ nanosheets can be as large as 40 μm, and the thickness can be as thin as 3.8 nm. The pure tetragonal phase can be obtained when the composition of $FeTe_{1-x}Se_x$ is tuned from x= 0 to 0.7. Further cryogenic electrical measurements confirmed the existence of superconductivity in these nanosheets. Besides, in another work reported by Gong et al.,[67] the superconducting oxygen doped-FeTe was also prepared by the CVD method. The CVD-grown superconducting TMCs possess several key advantages, including controllable thickness, large grain size, and high quality.

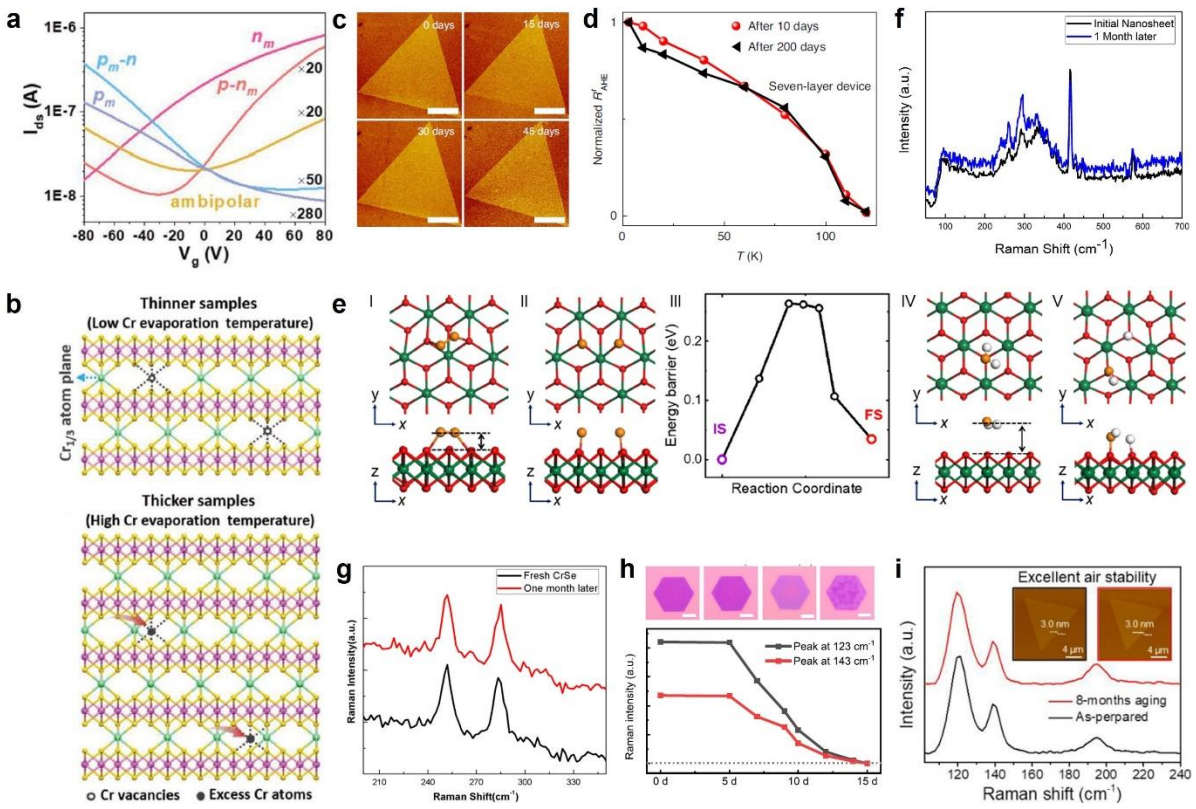

Figure 12. (a-b) Thickness-dependent electrical properties of Cr_2S_3 nanosheets: (a) Transfer curves (I_{ds}–V_g) of the transistors based on Cr_2S_3 flakes with different thicknesses. (b) Side view of the atomic model of thinner and thicker rhombohedral Cr_2S_3. Reproduced with permission from ref 41. Copyright 2019. Wiley-VCH.[41] (c-d) Stability test of CVD-grown 2D $CrSe_2$: (c) AFM images of monolayer $CrSe_2$ after exposure in air for different lengths of time. Scale bar: 3 μm. (d) Magnetotransport measurements of devices based on seven-layer $CrSe_2$ nanosheets after 10 days and 200 days' exposure in air. (e) Physisorption and chemisorption of O_2 and H_2O on 2D $CrSe_2$. Reproduced with permission from ref 40. Copyright 2021, Springer Nature.[40] (f-g) Time-dependent Raman spectra of CVD-grown Cr_2S_3 (f) and CrSe (g) nanosheets. Reproduced with permission from ref 50 and 52. Copyright 2019, American Chemical Society.[50] Copyright 2019. Wiley-VCH.[52] (h) Optical images and corresponding Raman intensities of 4 nm-thick $CrTe_2$ exposed in ambient conditions for various days. Scale bar: 20 μm. Reproduced with permission from ref 51. Copyright 2021, Springer Nature.[51] (i) Raman spectra and corresponding AFM images of CVD-grown Cr_5Te_8 nanoflakes before and after exposure in air for 8 months. Reproduced with permission from ref 58. Copyright 2021. Wiley-VCH.[58]

5. Stability of 2D magnetic TMCs

Although various 2D magnetic TMCs have been successfully prepared by controlling the

growth kinetics, further evaluation of their ambient stability is crucial for fundamental studies and potential industrial applications. To illustrate, the well-studied $Cr_2Ge_2Te_6$, Fe_3GeTe_2, and CrI_3 have demonstrated a range of fascinating ferromagnetic properties, but are seriously hindered by the extreme environmental sensitivity.

Most Cr_mX_n explored so far demonstrate excellent environmental stability, which is ideal for intrinsic magnetism exploration and practical applications. Figure 12c shows the AFM images of $CrSe_2$ exposed to air for 45 days, exhibiting no apparent change to the sample morphology and thickness.[40] Moreover, Li and co-workers also conducted the magnetotransport study on the seven-layer $CrSe_2$-based device after 10 days and 200 days of air exposure. Little change in the normalized R^r_{AHE} of the $CrSe_2$ device was identified (Figure 12d), further demonstrating the outstanding air stability of the material. The robustness of $CrSe_2$ against O_2 and H_2O was revealed by theoretical calculations as well (Figure 12e). It is found that the dissociative adsorption of O_2 and H_2O, as a key step in materials degradation, is endothermic with energy rises of 0.04 eV and 0.44 eV, respectively. The positive formation enthalpy hinders reactions occurring under normal conditions, giving rise to great stability of $CrSe_2$ in air. Not only $CrSe_2$, CrSe and Cr_2S_3 were determined to possess excellent stability as well, as evidenced by the time-dependent Raman spectra (Figure 12f-g).[50, 52]

Despite the general sensitivity of tellurides, chromium tellurides are surprisingly stable in the ambient condition, as confirmed by various research groups.[51, 58] $CrTe_2$, for instance, was found to have good air stability. Meng et al. monitored and studied few-layered $CrTe_2$ exposed to the ambient environment for 15 days.[51] As shown in Figure 12h, the morphology, color, and characteristic Raman peak intensities of few-layered $CrTe_2$ remain almost unchanged even after exposure to air for five days, indicating that the obtained 1T-$CrTe_2$ samples preserve high crystallinity against the ambient exposure. Furthermore, by continuously tracking the structure

and surface feature variation over eight months of aging in ambient air, Chen et al. evaluated the air stability of the 2D CVD-grown Cr_5Te_8.[58] The combined Raman spectra and AFM images demonstrate excellent air stability of the Cr_5Te_8 flakes (Figure 12i).

In the case of iron chalcogenides, CVD synthesized Fe_7Se_8 nanocrystals are reported to be stable, with their Raman spectra unchanged after one month and MFM signals unchanged after two hours in the ambient atmosphere.[42] On the contrary, FeTe nanocrystals prepared by the CVD method seemed to be very unstable. Evident changes in optical images can be observed even after half an hour in the ambient atmosphere. The stability issue could be a reason why different magnetic properties of this material were reported. This also requires us to be very careful when characterizing the structure and unveiling the intrinsic magnetic properties of FeTe.

6. Conclusions and Outlook

In the past few years, there have been many breakthroughs in the controllable CVD synthesis of 2D magnetic TMCs. Numerous fascinating magnetic phenomena in 2D TMCs due to the existence of rich phases have been unraveled and investigated. This review provides a comprehensive overview of the state-of-the-art research activities in the preparation of magnetic 2D TMCs and exploration of their intriguing structures and properties. The reported synthesis conditions and resulting structures of CVD-grown Cr_mX_n, Fe_mX_n, V_mX_n, and Mn_mX_n are summarized and compared. The effects of key CVD parameters on the sample morphology and phase, such as growth temperature, deposition time, and carrier gas, are particularly introduced and discussed. Importantly, several interesting magnetic properties identified in 2D TMCs are summarized and discussed, including magnetic anisotropy, thickness dependency, phase dependency, and anomalous magnetoresistance. As one of the most important

considerations for the potential application of 2D magnets, the stabilities of novel magnetic 2D TMCs are also elaborated on.

The current achievements have demonstrated that the CVD method is a powerful and reliable tool in achieving the synthesis of ultrathin magnetic TMCs with controllable phases, which might exhibit new properties undiscovered in their bulk counterparts due to the structure distortion, quantum confinement, and largely increased surface states in 2D form. At the same time, there is still plenty of room for further studies. The complexity of the CVD method makes the current successful examples mainly limited to single binary materials. For future applications in spintronics, there is a need to develop more synthesizable materials with diverse magnetic properties and prepare heterostructure based on different kinds of materials. In addition, the magnetic properties of materials are intrinsically sensitive to crystal defects, where the local magnetic properties could differ from the bulk sites. This provides a way to manipulate the magnetic properties of materials by defect engineering. Further studies can be carried out to control the defects in materials and understand their relationship to the magnetic properties. Besides, the successful practice of CVD methods highly relies on the experiences of the user. As can be seen, different kinds of CVD setup and parameters were used in the synthesis of 2D magnetic TMCs, while there are no quantitative ways to precisely describe how these synthetic parameters would affect the products in the materials. Considering the complexity of the CVD, more effective simulation methods are needed to further understand the processes. In addition, the rapidly developing machine learning methods can also be powerful tools to effectively develop the recipe to prepare large-scale and high-quality 2D magnetic TMCs for application in spintronics.

For the practical application of 2D magnetic TMCs, the relatively low T_C and small size are big challenges. So far, most synthesized 2D magnetic TMCs show long-range magnetic order

at a lower temperature due to the effect of structural defects and impurities. Thus, it is necessary to improve the crystal quality to obtain more 2D magnetic TMCs with T_C higher than room temperature. The robust synthesis of large-scale 2D magnetic TMCs with uniform ferromagnetism also needs to be developed from the view of practical application. In addition, integrating 2D magnetic TMCs with other 2D materials into heterostructures through the CVD strategy provides another path to engineering new structures with exciting magnetic properties for spintronic applications. We believe that the CVD method has its unique advantages in preparing 2D magnetic materials, which provides us a fantastic platform to study and engineer the magnetic properties in 2D nanomaterials. Rich opportunities and fruits are awaiting discovery.

AUTHOR INFORMATION

Corresponding Authors

Xiaowei Wang - *School of Materials Science and Engineering, Nanyang Technological University, Singapore 639798, Singapore; i-Lab, Key Laboratory of Multifunctional Nanomaterials and Smart Systems, Suzhou Institute of NanoTech and Nano-Bionics, Chinese Academy of Sciences, Suzhou 215123, China;* Email: wangxiaowei@ntu.edu.sg

Zheng Liu - *School of Materials Science and Engineering, Nanyang Technological University, Singapore. CINTRA CNRS/NTU/THALES, UMI 3288, Research Techno Plaza, 50 Nanyang Drive, Border X Block, Level 6. School of Electrical and Electronic Engineering, Nanyang Technological University, Singapore 639798, Singapore;* Email: z.liu@ntu.edu.sg

Authors

Bijun Tang‡ − *School of Materials Science and Engineering, Nanyang Technological University, Singapore 639798, Singapore.*

Dianyi Hu‡ − *School of Materials Science and Engineering, Nanyang Technological University, Singapore 639798, Singapore.*

Xiaoxu Zhao − *School of Materials Science and Engineering, Nanyang Technological University, Singapore 639798, Singapore.*

Author Contributions

The manuscript was written through contributions of all authors. All authors have given approval to the final version of the manuscript. ‡These authors contributed equally.

Notes

The authors declare no competing financial interest.

ACKNOWLEDGMENT

Z.L. acknowledges support from National Research Foundation Singapore programme NRF-CRP22-2019-0007 and NRF-CRP21-2018-0007. This research is also supported by the Ministry of Education, Singapore, under its AcRF Tier 3 Programme 'Geometrical Quantum Materials' (MOE2018-T3-1-002), and AcRF Tier 1 RG161/19.

REFERENCES

(1) Wang, Q. H.; Kalantar-Zadeh, K.; Kis, A.; Coleman, J. N.; Strano, M. S. Electronics and optoelectronics of two-dimensional transition metal dichalcogenides. *Nature nanotechnology* **2012**, *7* (11), 699.

(2) Chen, Y.; Fan, Z.; Zhang, Z.; Niu, W.; Li, C.; Yang, N.; Chen, B.; Zhang, H. Two-dimensional metal nanomaterials: synthesis, properties, and applications. *Chemical reviews* **2018**, *118* (13), 6409-6455.

(3) Chhowalla, M.; Shin, H. S.; Eda, G.; Li, L.-J.; Loh, K. P.; Zhang, H. The chemistry of two-dimensional layered transition metal dichalcogenide nanosheets. *Nature chemistry* **2013**, *5* (4),

263.
(4) Gong, C.; Zhang, X. Two-dimensional magnetic crystals and emergent heterostructure devices. *Science* **2019**, *363* (6428), eaav4450.
(5) Lin, X.; Yang, W.; Wang, K. L.; Zhao, W. Two-dimensional spintronics for low-power electronics. *Nature Electronics* **2019**, *2* (7), 274-283.
(6) Chang, C.; Chen, W.; Chen, Y.; Chen, Y.; Chen, Y.; Ding, F.; Fan, C.; Fan, H. J.; Fan, Z.; Gong, C. Recent progress on two-dimensional materials. *Acta Physico-Chimica Sinica* **2021**, *37* (12), 2108017.
(7) Schaibley, J. R.; Yu, H.; Clark, G.; Rivera, P.; Ross, J. S.; Seyler, K. L.; Yao, W.; Xu, X. Valleytronics in 2D materials. *Nature Reviews Materials* **2016**, *1* (11), 1-15.
(8) Jiang, H.; Zheng, L.; Liu, Z.; Wang, X. Two-dimensional materials: From mechanical properties to flexible mechanical sensors. *InfoMat* **2020**, *2* (6), 1077-1094.
(9) Gibertini, M.; Koperski, M.; Morpurgo, A.; Novoselov, K. Magnetic 2D materials and heterostructures. *Nature nanotechnology* **2019**, *14* (5), 408-419.
(10) Burch, K. S.; Mandrus, D.; Park, J.-G. Magnetism in two-dimensional van der Waals materials. *Nature* **2018**, *563* (7729), 47-52.
(11) Huang, B.; Clark, G.; Navarro-Moratalla, E.; Klein, D. R.; Cheng, R.; Seyler, K. L.; Zhong, D.; Schmidgall, E.; McGuire, M. A.; Cobden, D. H. Layer-dependent ferromagnetism in a van der Waals crystal down to the monolayer limit. *Nature* **2017**, *546* (7657), 270-273.
(12) Gong, C.; Li, L.; Li, Z.; Ji, H.; Stern, A.; Xia, Y.; Cao, T.; Bao, W.; Wang, C.; Wang, Y. Discovery of intrinsic ferromagnetism in two-dimensional van der Waals crystals. *Nature* **2017**, *546* (7657), 265-269.
(13) Fei, Z.; Huang, B.; Malinowski, P.; Wang, W.; Song, T.; Sanchez, J.; Yao, W.; Xiao, D.; Zhu, X.; May, A. F. Two-dimensional itinerant ferromagnetism in atomically thin Fe_3GeTe_2. *Nature materials* **2018**, *17* (9), 778-782.
(14) Deng, Y.; Yu, Y.; Song, Y.; Zhang, J.; Wang, N. Z.; Sun, Z.; Yi, Y.; Wu, Y. Z.; Wu, S.; Zhu, J. Gate-tunable room-temperature ferromagnetism in two-dimensional Fe_3GeTe_2. *Nature* **2018**, *563* (7729), 94-99.
(15) Klein, D. R.; MacNeill, D.; Lado, J. L.; Soriano, D.; Navarro-Moratalla, E.; Watanabe, K.; Taniguchi, T.; Manni, S.; Canfield, P.; Fernández-Rossier, J. Probing magnetism in 2D van der Waals crystalline insulators via electron tunneling. *Science* **2018**, *360* (6394), 1218-1222.
(16) Huang, B.; Clark, G.; Klein, D. R.; MacNeill, D.; Navarro-Moratalla, E.; Seyler, K. L.; Wilson, N.; McGuire, M. A.; Cobden, D. H.; Xiao, D. Electrical control of 2D magnetism in bilayer CrI3. *Nature nanotechnology* **2018**, *13* (7), 544-548.

(17) Jiang, S.; Li, L.; Wang, Z.; Mak, K. F.; Shan, J. Controlling magnetism in 2D CrI3 by electrostatic doping. *Nature nanotechnology* **2018**, *13* (7), 549-553.
(18) Wang, Z.; Zhang, T.; Ding, M.; Dong, B.; Li, Y.; Chen, M.; Li, X.; Huang, J.; Wang, H.; Zhao, X. Electric-field control of magnetism in a few-layered van der Waals ferromagnetic semiconductor. *Nature nanotechnology* **2018**, *13* (7), 554-559.
(19) Li, H.; Ruan, S.; Zeng, Y. J. Intrinsic van der Waals magnetic materials from bulk to the 2D limit: new frontiers of spintronics. *Advanced Materials* **2019**, *31* (27), 1900065.
(20) Zhou, J.; Lin, J.; Huang, X.; Zhou, Y.; Chen, Y.; Xia, J.; Wang, H.; Xie, Y.; Yu, H.; Lei, J. A library of atomically thin metal chalcogenides. *Nature* **2018**, *556* (7701), 355-359.
(21) Cai, Z.; Liu, B.; Zou, X.; Cheng, H.-M. Chemical vapor deposition growth and applications of two-dimensional materials and their heterostructures. *Chemical reviews* **2018**, *118* (13), 6091-6133.
(22) Li, H.; Li, Y.; Aljarb, A.; Shi, Y.; Li, L.-J. Epitaxial growth of two-dimensional layered transition-metal dichalcogenides: growth mechanism, controllability, and scalability. *Chemical reviews* **2017**, *118* (13), 6134-6150.
(23) Zhang, J.; Wang, F.; Shenoy, V. B.; Tang, M.; Lou, J. Towards controlled synthesis of 2D crystals by chemical vapor deposition (CVD). *Materials Today* **2020**, *40*, 132-139.
(24) Tang, B.; Che, B.; Xu, M.; Ang, Z. P.; Di, J.; Gao, H.-J.; Yang, H.; Zhou, J.; Liu, Z. Recent advances in synthesis and study of 2D twisted transition metal dichalcogenide bilayers. *Small Structures* **2021**, *2* (5), 2000153.
(25) Shi, Y.; Li, H.; Li, L.-J. Recent advances in controlled synthesis of two-dimensional transition metal dichalcogenides via vapour deposition techniques. *Chemical Society Reviews* **2015**, *44* (9), 2744-2756.
(26) Ji, Q.; Zhang, Y.; Zhang, Y.; Liu, Z. Chemical vapour deposition of group-VIB metal dichalcogenide monolayers: engineered substrates from amorphous to single crystalline. *Chemical Society Reviews* **2015**, *44* (9), 2587-2602.
(27) Shivayogimath, A.; Thomsen, J. D.; Mackenzie, D.; Geisler, M.; Stan, R.-M.; Holt, A. J.; Bianchi, M.; Crovetto, A.; Whelan, P. R.; Carvalho, A. A universal approach for the synthesis of two-dimensional binary compounds. *Nature communications* **2019**, *10* (1), 1-7.
(28) Lee, Y. H.; Zhang, X. Q.; Zhang, W.; Chang, M. T.; Lin, C. T.; Chang, K. D.; Yu, Y. C.; Wang, J. T. W.; Chang, C. S.; Li, L. J. Synthesis of large-area MoS2 atomic layers with chemical vapor deposition. *Advanced materials* **2012**, *24* (17), 2320-2325.
(29) Gao, Y.; Liu, Z.; Sun, D.-M.; Huang, L.; Ma, L.-P.; Yin, L.-C.; Ma, T.; Zhang, Z.; Ma, X.-L.; Peng, L.-M. Large-area synthesis of high-quality and uniform monolayer WS 2 on

reusable Au foils. *Nature communications* **2015**, *6*, 8569.
(30) Gong, Y.; Ye, G.; Lei, S.; Shi, G.; He, Y.; Lin, J.; Zhang, X.; Vajtai, R.; Pantelides, S. T.; Zhou, W. Synthesis of Millimeter-Scale Transition Metal Dichalcogenides Single Crystals. *Advanced Functional Materials* **2016**, *26* (12), 2009-2015.
(31) Zhou, J.; Liu, F.; Lin, J.; Huang, X.; Xia, J.; Zhang, B.; Zeng, Q.; Wang, H.; Zhu, C.; Niu, L. Large-area and high-quality 2D transition metal telluride. *Advanced Materials* **2017**, *29* (3), 1603471.
(32) Chen, K.; Chen, Z.; Wan, X.; Zheng, Z.; Xie, F.; Chen, W.; Gui, X.; Chen, H.; Xie, W.; Xu, J. A Simple Method for Synthesis of High-Quality Millimeter-Scale 1T′ Transition-Metal Telluride and Near-Field Nanooptical Properties. *Advanced Materials* **2017**, *29* (38), 1700704.
(33) Choi, W.; Choudhary, N.; Han, G. H.; Park, J.; Akinwande, D.; Lee, Y. H. Recent development of two-dimensional transition metal dichalcogenides and their applications. *Materials Today* **2017**, *20* (3), 116-130.
(34) Gong, Y.-J.; Liu, Z. Preface to the special issue on tungsten-and molybdenum-based two-dimensional materials for energy storage and conversion. Springer: 2020; Vol. 2, pp 107-108.
(35) Zheng, L.; Wang, X.; Jiang, H.; Xu, M.; Huang, W.; Liu, Z. Recent progress of flexible electronics by 2D transition metal dichalcogenides. *Nano Research* **2021**, 1-20.
(36) Ruihuan Duan, Y. D., Jiefu Yang, Zheng Liu. High-Quality 2D TMD Crystals Synthesized by Solid-state Reaction in Vacuum System and Their Applications. *Chinese Journal of Vacuum Science and Technology* **2021**, *41* (1), 1-21.
(37) Li, J.; Zhao, B.; Chen, P.; Wu, R.; Li, B.; Xia, Q.; Guo, G.; Luo, J.; Zang, K.; Zhang, Z. Synthesis of Ultrathin Metallic MTe2 (M= V, Nb, Ta) Single-Crystalline Nanoplates. *Advanced Materials* **2018**, *30* (36), 1801043.
(38) Bonilla, M.; Kolekar, S.; Ma, Y.; Diaz, H. C.; Kalappattil, V.; Das, R.; Eggers, T.; Gutierrez, H. R.; Phan, M.-H.; Batzill, M. Strong room-temperature ferromagnetism in VSe_2 monolayers on van der Waals substrates. *Nature nanotechnology* **2018**, *13* (4), 289-293.
(39) Kang, L.; Ye, C.; Zhao, X.; Zhou, X.; Hu, J.; Li, Q.; Liu, D.; Das, C. M.; Yang, J.; Hu, D. Phase-controllable growth of ultrathin 2D magnetic FeTe crystals. *Nature communications* **2020**, *11* (1), 1-9.
(40) Li, B.; Wan, Z.; Wang, C.; Chen, P.; Huang, B.; Cheng, X.; Qian, Q.; Li, J.; Zhang, Z.; Sun, G. Van der Waals epitaxial growth of air-stable $CrSe_2$ nanosheets with thickness-tunable magnetic order. *Nature Materials* **2021**, 1-8.
(41) Cui, F.; Zhao, X.; Xu, J.; Tang, B.; Shang, Q.; Shi, J.; Huan, Y.; Liao, J.; Chen, Q.; Hou, Y. Controlled Growth and Thickness-Dependent Conduction-Type Transition of 2D

Ferrimagnetic Cr_2S_3 Semiconductors. *Advanced Materials* **2020**, *32* (4), 1905896.
(42) Zhao, Z.; Zhou, J.; Liu, L.; Liu, N.; Huang, J.; Zhang, B.; Li, W.; Zeng, Y.; Zhang, T.; Ji, W.; Yang, T.; Zhang, Z.; Li, S.; Hou, Y. Two-Dimensional Room-Temperature Magnetic Nonstoichiometric Fe7Se8 Nanocrystals: Controllable Synthesis and Magnetic Behavior. *Nano Lett.* **2022**, *22* (3), 1242-1250. DOI: 10.1021/acs.nanolett.1c04403.
(43) O'Hara, D. J.; Zhu, T.; Trout, A. H.; Ahmed, A. S.; Luo, Y. K.; Lee, C. H.; Brenner, M. R.; Rajan, S.; Gupta, J. A.; McComb, D. W. Room temperature intrinsic ferromagnetism in epitaxial manganese selenide films in the monolayer limit. *Nano letters* **2018**, *18* (5), 3125-3131.
(44) Niu, J.; Yan, B.; Ji, Q.; Liu, Z.; Li, M.; Gao, P.; Zhang, Y.; Yu, D.; Wu, X. Anomalous Hall effect and magnetic orderings in nanothick V5S8. *Physical Review B* **2017**, *96* (7), 075402.
(45) Liu, H.; Bao, L.; Zhou, Z.; Che, B.; Zhang, R.; Bian, C.; Ma, R.; Wu, L.; Yang, H.; Li, J. Quasi-2D transport and weak antilocalization effect in few-layered VSe2. *Nano Letters* **2019**, *19* (7), 4551-4559.
(46) Li, S.; Wu, J.; Liang, B.; Liu, L.; Zhang, W.; Wazir, N.; Zhou, J.; Liu, Y.; Nie, Y.; Hao, Y. Antiferromagnetic α-MnTe: Molten-Salt-Assisted Chemical Vapor Deposition Growth and Magneto-Transport Properties. *Chemistry of Materials* **2022**, *34* (2), 873-880.
(47) Lee, J.-U.; Lee, S.; Ryoo, J. H.; Kang, S.; Kim, T. Y.; Kim, P.; Park, C.-H.; Park, J.-G.; Cheong, H. Ising-type magnetic ordering in atomically thin FePS3. *Nano letters* **2016**, *16* (12), 7433-7438.
(48) Jiang, X.; Liu, Q.; Xing, J.; Liu, N.; Guo, Y.; Liu, Z.; Zhao, J. Recent progress on 2D magnets: Fundamental mechanism, structural design and modification. *Applied Physics Reviews* **2021**, *8* (3), 031305.
(49) Li, W.; Qiu, X.; Lv, B.; Zhang, B.; Tang, J.; Xu, J.; Tian, K.; Zhao, Z.; Zeng, Y.; Huang, X. Free-standing 2D ironene with magnetic vortex structure at room temperature. *Matter* **2022**, *5* (1), 291-301.
(50) Chu, J.; Zhang, Y.; Wen, Y.; Qiao, R.; Wu, C.; He, P.; Yin, L.; Cheng, R.; Wang, F.; Wang, Z. Sub-millimeter-scale growth of one-unit-cell-thick ferrimagnetic Cr_2S_3 nanosheets. *Nano letters* **2019**, *19* (3), 2154-2161.
(51) Meng, L.; Zhou, Z.; Xu, M.; Yang, S.; Si, K.; Liu, L.; Wang, X.; Jiang, H.; Li, B.; Qin, P. Anomalous thickness dependence of Curie temperature in air-stable two-dimensional ferromagnetic 1T-$CrTe_2$ grown by chemical vapor deposition. *Nature communications* **2021**, *12* (1), 1-8.
(52) Zhang, Y.; Chu, J.; Yin, L.; Shifa, T. A.; Cheng, Z.; Cheng, R.; Wang, F.; Wen, Y.; Zhan,

X.; Wang, Z. Ultrathin Magnetic 2D Single-Crystal CrSe. *Advanced Materials* **2019**, *31* (19), 1900056.
(53) Tang, B.; Wang, X.; Han, M.; Xu, X.; Zhang, Z.; Zhu, C.; Cao, X.; Yang, Y.; Fu, Q.; Yang, J. Phase engineering of Cr5Te8 with colossal anomalous Hall effect. *Nature Electronics* **2022**, *5* (4), 224-232.
(54) Wang, M.; Kang, L.; Su, J.; Zhang, L.; Dai, H.; Cheng, H.; Han, X.; Zhai, T.; Liu, Z.; Han, J. Two-dimensional ferromagnetism in CrTe flakes down to atomically thin layers. *Nanoscale* **2020**, *12* (31), 16427-16432.
(55) Zhou, S.; Wang, R.; Han, J.; Wang, D.; Li, H.; Gan, L.; Zhai, T. Ultrathin non-van der Waals magnetic Rhombohedral Cr_2S_3: space-confined chemical vapor deposition synthesis and raman scattering investigation. *Advanced Functional Materials* **2019**, *29* (3), 1805880.
(56) Coughlin, A. L.; Xie, D.; Yao, Y.; Zhan, X.; Chen, Q.; Hewa-Walpitage, H.; Zhang, X.; Guo, H.; Zhou, H.; Lou, J. Near Degeneracy of Magnetic Phases in Two-Dimensional Chromium Telluride with Enhanced Perpendicular Magnetic Anisotropy. *ACS nano* **2020**, *14* (11), 15256-15266.
(57) Wen, Y.; Liu, Z.; Zhang, Y.; Xia, C.; Zhai, B.; Zhang, X.; Zhai, G.; Shen, C.; He, P.; Cheng, R. Tunable Room-temperature Ferromagnetism in two-dimensional Cr_2Te_3. *Nano Letters* **2020**, *20* (5), 3130-3139.
(58) Chen, C.; Chen, X.; Wu, C.; Wang, X.; Ping, Y.; Wei, X.; Zhou, X.; Lu, J.; Zhu, L.; Zhou, J. Air-Stable 2D Cr5Te8 Nanosheets with Thickness-Tunable Ferromagnetism. *Advanced Materials* **2022**, *34* (2), 2107512.
(59) Krivanek, O. L.; Chisholm, M. F.; Nicolosi, V.; Pennycook, T. J.; Corbin, G. J.; Dellby, N.; Murfitt, M. F.; Own, C. S.; Szilagyi, Z. S.; Oxley, M. P. Atom-by-atom structural and chemical analysis by annular dark-field electron microscopy. *Nature* **2010**, *464* (7288), 571-574.
(60) Zhao, X.; Ning, S.; Fu, W.; Pennycook, S. J.; Loh, K. P. Differentiating polymorphs in molybdenum disulfide via electron microscopy. *Advanced Materials* **2018**, *30* (47), 1802397.
(61) Matthews, P. D.; Akhtar, M.; Malik, M. A.; Revaprasadu, N.; O'Brien, P. Synthetic routes to iron chalcogenide nanoparticles and thin films. *Dalton Transactions* **2016**, *45* (47), 18803-18812.
(62) Oyler, K. D.; Ke, X.; Sines, I. T.; Schiffer, P.; Schaak, R. E. Chemical synthesis of two-dimensional iron chalcogenide nanosheets: FeSe, FeTe, Fe (Se, Te), and FeTe2. *Chemistry of Materials* **2009**, *21* (15), 3655-3661.
(63) Liu, A.; Chen, X.; Zhang, Z.; Jiang, Y.; Shi, C. Selective synthesis and magnetic properties

of FeSe2 and FeTe2 nanocrystallites obtained through a hydrothermal co-reduction route. *Solid state communications* **2006**, *138* (10-11), 538-541.
(64) Ma, F.; Ji, W.; Hu, J.; Lu, Z.-Y.; Xiang, T. First-principles calculations of the electronic structure of tetragonal α-FeTe and α-FeSe crystals: evidence for a bicollinear antiferromagnetic order. *Physical review letters* **2009**, *102* (17), 177003.
(65) Koz, C.; Rößler, S.; Tsirlin, A. A.; Wirth, S.; Schwarz, U. Low-temperature phase diagram of Fe1+yTe studied using x-ray diffraction. *Physical Review B* **2013**, *88* (9), 094509.
(66) Böhmer, A.; Arai, T.; Hardy, F.; Hattori, T.; Iye, T.; Wolf, T.; Löhneysen, H. v.; Ishida, K.; Meingast, C. Origin of the tetragonal-to-orthorhombic phase transition in FeSe: A combined thermodynamic and NMR study of nematicity. *Physical review letters* **2015**, *114* (2), 027001.
(67) Wang, X.; Bian, C.; He, Y.; Guo, J.; Zhang, P.; Liu, L.; Wei, Y.; Meng, L.; Jiang, H.; Li, B. Ultrathin FeTe nanosheets with tetragonal and hexagonal phases synthesized by chemical vapor deposition. *Materials Today* **2021**, *45*, 35-43.
(68) Zhang, H.; Li, Q.; Hossain, M.; Li, B.; Chen, K.; Huang, Z.; Yang, X.; Dang, W.; Shu, W.; Wang, D. Phase-Selective Synthesis of Ultrathin FeTe Nanoplates by Controllable Fe/Te Atom Ratio in the Growth Atmosphere. *Small* **2021**, *17* (33), 2101616.
(69) Chen, S.; Liu, H.; Chen, F.; Zhou, K.; Xue, Y. Synthesis, Transfer, and Properties of Layered FeTe2 Nanocrystals. *ACS nano* **2020**, *14* (9), 11473-11481.
(70) Cheng, M.; Zhao, X.; Zeng, Y.; Wang, P.; Wang, Y.; Wang, T.; Pennycook, S. J.; He, J.; Shi, J. Phase-Tunable Synthesis and Etching-Free Transfer of Two-Dimensional Magnetic FeTe. *ACS nano* **2021**, *15* (12), 19089-19097.
(71) Capitano, D.; Hu, Z.; Liu, Y.; Tong, X.; Nykypanchuk, D.; DiMarzio, D.; Petrovic, C. Synthesis and Characterization of Ultrathin FeTe2 Nanocrystals. *ACS omega* **2021**, *6* (16), 10537-10546.
(72) Liu, H.; Xue, Y. Van Der Waals epitaxial growth and phase transition of layered FeSe2 nanocrystals. *Advanced Materials* **2021**, *33* (17), 2008456.
(73) Wang, X.; Bian, C.; He, Y.; Guo, J.; Zhang, P.; Liu, L.; Wei, Y.; Meng, L.; Jiang, H.; Li, B.; Nie, A.; Bao, L.; Gong, Y. Ultrathin FeTe nanosheets with tetragonal and hexagonal phases synthesized by chemical vapor deposition. *Mater. Today* **2021**, *45*, 35-43. DOI: https://doi.org/10.1016/j.mattod.2020.11.022.
(74) Nair, G. K. R.; Zhang, Z.; Hou, F.; Abdelaziem, A.; Xu, X.; Yang, S. W. Q.; Zhang, N.; Li, W.; Zhu, C.; Wu, Y.; Weiling, H.; Kang, L.; Salim, T.; Zhou, J.; Ke, L.; Lin, J.; Li, X.; Gao, W.; Liu, Z. Phase-pure two-dimensional FexGeTe2 magnets with near-room-temperature TC.

Nano Res. **2022**, *15* (1), 457-464. DOI: 10.1007/s12274-021-3502-0.

(75) Zhang, H.; Li, Q.; Hossain, M.; Li, B.; Chen, K.; Huang, Z.; Yang, X.; Dang, W.; Shu, W.; Wang, D.; Li, B.; Xu, W.; Zhang, Z.; Yu, G.; Duan, X. Phase-Selective Synthesis of Ultrathin FeTe Nanoplates by Controllable Fe/Te Atom Ratio in the Growth Atmosphere. *Small* **2021**, *17* (33), 2101616. DOI: https://doi.org/10.1002/smll.202101616.

(76) Zhao, X.; Song, P.; Wang, C.; Riis-Jensen, A. C.; Fu, W.; Deng, Y.; Wan, D.; Kang, L.; Ning, S.; Dan, J.; Venkatesan, T.; Liu, Z.; Zhou, W.; Thygesen, K. S.; Luo, X.; Pennycook, S. J.; Loh, K. P. Engineering covalently bonded 2D layered materials by self-intercalation. *Nature* **2020**, *581* (7807), 171-177. DOI: 10.1038/s41586-020-2241-9.

(77) Najmaei, S.; Liu, Z.; Zhou, W.; Zou, X.; Shi, G.; Lei, S.; Yakobson, B. I.; Idrobo, J.-C.; Ajayan, P. M.; Lou, J. Vapour phase growth and grain boundary structure of molybdenum disulphide atomic layers. *Nature materials* **2013**, *12* (8), 754-759.

(78) Wang, S.; Rong, Y.; Fan, Y.; Pacios, M.; Bhaskaran, H.; He, K.; Warner, J. H. Shape evolution of monolayer MoS2 crystals grown by chemical vapor deposition. *Chemistry of Materials* **2014**, *26* (22), 6371-6379.

(79) Chen, J.; Liu, B.; Liu, Y.; Tang, W.; Nai, C. T.; Li, L.; Zheng, J.; Gao, L.; Zheng, Y.; Shin, H. S. Chemical Vapor Deposition of Large-Sized Hexagonal WSe2 Crystals on Dielectric Substrates. *Advanced materials* **2015**, *27* (42), 6722-6727.

(80) Gao, Y.; Liu, Z.; Sun, D.-M.; Huang, L.; Ma, L.-P.; Yin, L.-C.; Ma, T.; Zhang, Z.; Ma, X.-L.; Peng, L.-M. Large-area synthesis of high-quality and uniform monolayer WS2 on reusable Au foils. *Nature communications* **2015**, *6* (1), 1-10.

(81) Tang, B.; Lu, Y.; Zhou, J.; Chouhan, T.; Wang, H.; Golani, P.; Xu, M.; Xu, Q.; Guan, C.; Liu, Z. Machine learning-guided synthesis of advanced inorganic materials. *Materials Today* **2020**, *41*, 72-80.

(82) Zhou, J.; Tang, B.; Lin, J.; Lv, D.; Shi, J.; Sun, L.; Zeng, Q.; Niu, L.; Liu, F.; Wang, X. Morphology engineering in monolayer MoS2-WS2 lateral heterostructures. *Advanced Functional Materials* **2018**, *28* (31), 1801568.

(83) Guo, Y.; Kang, L.; Song, P.; Zeng, Q.; Tang, B.; Yang, J.; Wu, Y.; Tian, D.; Xu, M.; Zhao, W. MoO3–MoS2 vertical heterostructures synthesized via one-step CVD process for optoelectronics. *2D Materials* **2021**, *8* (3), 035036.

(84) Coughlin, A. L.; Xie, D.; Zhan, X.; Yao, Y.; Deng, L.; Hewa-Walpitage, H.; Bontke, T.; Chu, C.-W.; Li, Y.; Wang, J. Van der Waals Superstructure and Twisting in Self-Intercalated Magnet with Near Room-Temperature Perpendicular Ferromagnetism. *Nano letters* **2021**, *21* (22), 9517-9525.

(85) Li, S.; Lin, Y.-C.; Zhao, W.; Wu, J.; Wang, Z.; Hu, Z.; Shen, Y.; Tang, D.-M.; Wang, J.; Zhang, Q. Vapour–liquid–solid growth of monolayer MoS2 nanoribbons. *Nature materials* **2018**, *17* (6), 535-542.

(86) Yang, P.; Zou, X.; Zhang, Z.; Hong, M.; Shi, J.; Chen, S.; Shu, J.; Zhao, L.; Jiang, S.; Zhou, X. Batch production of 6-inch uniform monolayer molybdenum disulfide catalyzed by sodium in glass. *Nature communications* **2018**, *9* (1), 1-10.

(87) Tang, B.; Zhou, J.; Sun, P.; Wang, X.; Bai, L.; Dan, J.; Yang, J.; Zhou, K.; Zhao, X.; Pennycook, S. J. Phase-controlled synthesis of monolayer ternary telluride with a random local displacement of tellurium atoms. *Advanced Materials* **2019**, *31* (23), 1900862.

(88) Cui, F.; Wang, C.; Li, X.; Wang, G.; Liu, K.; Yang, Z.; Feng, Q.; Liang, X.; Zhang, Z.; Liu, S. Tellurium-assisted epitaxial growth of large-area, highly crystalline ReS2 atomic layers on mica substrate. *Advanced Materials* **2016**, *28* (25), 5019-5024.

(89) Utama, M. I. B.; Zhang, Q.; Zhang, J.; Yuan, Y.; Belarre, F. J.; Arbiol, J.; Xiong, Q. Recent developments and future directions in the growth of nanostructures by van der Waals epitaxy. *Nanoscale* **2013**, *5* (9), 3570-3588.

(90) Zhang, Z.; Niu, J.; Yang, P.; Gong, Y.; Ji, Q.; Shi, J.; Fang, Q.; Jiang, S.; Li, H.; Zhou, X. Van der Waals epitaxial growth of 2D metallic vanadium diselenide single crystals and their extra-high electrical conductivity. *Advanced Materials* **2017**, *29* (37), 1702359.

(91) Zheng, B.; Chen, Y.; Wang, Z.; Qi, F.; Huang, Z.; Hao, X.; Li, P.; Zhang, W.; Li, Y. Vertically oriented few-layered HfS2 nanosheets: growth mechanism and optical properties. *2D Materials* **2016**, *3* (3), 035024.

(92) Li, X.; Cui, F.; Feng, Q.; Wang, G.; Xu, X.; Wu, J.; Mao, N.; Liang, X.; Zhang, Z.; Zhang, J. Controlled growth of large-area anisotropic ReS2 atomic layer and its photodetector application. *Nanoscale* **2016**, *8* (45), 18956-18962.

(93) Liu, B.; Fathi, M.; Chen, L.; Abbas, A.; Ma, Y.; Zhou, C. Chemical vapor deposition growth of monolayer WSe2 with tunable device characteristics and growth mechanism study. *ACS nano* **2015**, *9* (6), 6119-6127.

(94) He, Y.; Sobhani, A.; Lei, S.; Zhang, Z.; Gong, Y.; Jin, Z.; Zhou, W.; Yang, Y.; Zhang, Y.; Wang, X. Layer engineering of 2D semiconductor junctions. *Advanced Materials* **2016**, *28* (25), 5126-5132.

(95) Ma, H.; Chen, P.; Li, B.; Li, J.; Ai, R.; Zhang, Z.; Sun, G.; Yao, K.; Lin, Z.; Zhao, B. Thickness-tunable synthesis of ultrathin type-II Dirac semimetal PtTe2 single crystals and their thickness-dependent electronic properties. *Nano Letters* **2018**, *18* (6), 3523-3529.

(96) Zhao, B.; Dang, W.; Liu, Y.; Li, B.; Li, J.; Luo, J.; Zhang, Z.; Wu, R.; Ma, H.; Sun, G.

Synthetic control of two-dimensional NiTe2 single crystals with highly uniform thickness distributions. *Journal of the American Chemical Society* **2018**, *140* (43), 14217-14223.
(97) Xu, M.; Tang, B.; Lu, Y.; Zhu, C.; Lu, Q.; Zhu, C.; Zheng, L.; Zhang, J.; Han, N.; Fang, W. Machine Learning Driven Synthesis of Few-Layered WTe2 with Geometrical Control. *Journal of the American Chemical Society* **2021**, *143* (43), 18103-18113.
(98) You, J.; Hossain, M. D.; Luo, Z. Synthesis of 2D transition metal dichalcogenides by chemical vapor deposition with controlled layer number and morphology. *Nano Convergence* **2018**, *5* (1), 1-13.
(99) Wang, F.; Wang, Z.; Shifa, T. A.; Wen, Y.; Wang, F.; Zhan, X.; Wang, Q.; Xu, K.; Huang, Y.; Yin, L. Two-dimensional non-layered materials: synthesis, properties and applications. *Advanced Functional Materials* **2017**, *27* (19), 1603254.
(100) Parker, D. S. Strong 3D and 1D magnetism in hexagonal Fe-chalcogenides FeS and FeSe vs. weak magnetism in hexagonal FeTe. *Scientific Reports* **2017**, *7* (1), 1-6.
(101) Wang, R.; Yu, Y.; Zhou, S.; Li, H.; Wong, H.; Luo, Z.; Gan, L.; Zhai, T. Strategies on phase control in transition metal dichalcogenides. *Advanced Functional Materials* **2018**, *28* (47), 1802473.
(102) Ji, Q.; Li, C.; Wang, J.; Niu, J.; Gong, Y.; Zhang, Z.; Fang, Q.; Zhang, Y.; Shi, J.; Liao, L. Metallic vanadium disulfide nanosheets as a platform material for multifunctional electrode applications. *Nano Letters* **2017**, *17* (8), 4908-4916.
(103) Liu, H.; Xue, Y.; Shi, J.-A.; Guzman, R. A.; Zhang, P.; Zhou, Z.; He, Y.; Bian, C.; Wu, L.; Ma, R. Observation of the kondo effect in multilayer single-crystalline VTe2 nanoplates. *Nano Letters* **2019**, *19* (12), 8572-8580.
(104) Lee, S.; Kim, J.; Park, Y. C.; Chun, S.-H. Atomistic real-space observation of the van der Waals layered structure and tailored morphology in VSe2. *Nanoscale* **2019**, *11* (2), 431-436.
(105) Li, N.; Zhang, Y.; Cheng, R.; Wang, J.; Li, J.; Wang, Z.; Sendeku, M. G.; Huang, W.; Yao, Y.; Wen, Y. Synthesis and optoelectronic applications of a stable p-type 2D material: α-MnS. *ACS nano* **2019**, *13* (11), 12662-12670.
(106) Li, N.; Zhu, L.; Shang, H.; Wang, F.; Zhang, Y.; Yao, Y.; Wang, J.; Zhan, X.; Wang, F.; He, J. Controlled synthesis and Raman study of a 2D antiferromagnetic P-type semiconductor: α-MnSe. *Nanoscale* **2021**, *13* (14), 6953-6964.
(107) Hamasaki, T.; Hashimoto, T.; Yamaguchi, Y.; Watanabe, H. Neutron diffraction study of Cr2Te3 single crystal. *Solid State Communications* **1975**, *16* (7), 895-897.
(108) Wang, F.; Du, J.; Sun, F.; Sabirianov, R. F.; Al-Aqtash, N.; Sengupta, D.; Zeng, H.; Xu,

X. Ferromagnetic Cr2Te3 nanorods with ultrahigh coercivity. *Nanoscale* **2018**, *10* (23), 11028-11033.

(109) Wang, Y.; Yan, J.; Li, J.; Wang, S.; Song, M.; Song, J.; Li, Z.; Chen, K.; Qin, Y.; Ling, L. Magnetic anisotropy and topological Hall effect in the trigonal chromium tellurides Cr5Te8. *Physical Review B* **2019**, *100* (2), 024434.

(110) Yuzuri, M.; Kanomata, T.; Kaneko, T. The pressure effect on the Curie temperature and exchange striction of Cr2S3 and Cr2Te3. *Journal of Magnetism and Magnetic Materials* **1987**, *70* (1-3), 223-224.

(111) Kawaminami, M.; Okazaki, A. Neutron diffraction study of Fe7Se8. II. *Journal of the physical Society of Japan* **1970**, *29* (3), 649-655.

(112) Freitas, D. C.; Nunez, M.; Strobel, P.; Sulpice, A.; Weht, R.; Aligia, A. A.; Nunez-Regueiro, M. Antiferromagnetism and ferromagnetism in layered 1 T-CrSe2 with V and Ti replacements. *Physical Review B* **2013**, *87* (1), 014420.

(113) Hirone, T.; Chiba, S. On the magnetic anisotropy of single crystal of chromium telluride. *Journal of the Physical Society of Japan* **1960**, *15* (11), 1991-1994.

(114) Zhao, Z.; Zhou, J.; Liu, L.; Liu, N.; Huang, J.; Zhang, B.; Li, W.; Zeng, Y.; Zhang, T.; Ji, W. Two-Dimensional Room-Temperature Magnetic Nonstoichiometric Fe7Se8 Nanocrystals: Controllable Synthesis and Magnetic Behavior. *Nano Letters* **2022**, *22* (3), 1242-1250.

(115) Zhang, X.; Lu, Q.; Liu, W.; Niu, W.; Sun, J.; Cook, J.; Vaninger, M.; Miceli, P. F.; Singh, D. J.; Lian, S.-W. Room-temperature intrinsic ferromagnetism in epitaxial CrTe 2 ultrathin films. *Nature communications* **2021**, *12* (1), 1-9.

(116) Freitas, D. C.; Weht, R.; Sulpice, A.; Remenyi, G.; Strobel, P.; Gay, F.; Marcus, J.; Núñez-Regueiro, M. Ferromagnetism in layered metastable 1T-CrTe2. *Journal of Physics: Condensed Matter* **2015**, *27* (17), 176002.

(117) ANDRESEN, A. F.; Zeppezauer, E.; Boive, T.; Nordström, B.; Brändén, C. Magnetic structure of Cr 2 Te 3, Cr 3 Te 4, and Cr 5 Te 6. *Acta Chem. Scand.* **1970**, *24* (10), 3495-3509.

(118) Dijkstra, J.; Weitering, H.; Van Bruggen, C.; Haas, C.; De Groot, R. Band-structure calculations, and magnetic and transport properties of ferromagnetic chromium tellurides (CrTe, Cr3Te4, Cr2Te3). *Journal of Physics: Condensed Matter* **1989**, *1* (46), 9141.

(119) Akram, M.; Nazar, F. M. Magnetic properties of CrTe, Cr23Te24, Cr7Te8, Cr5Te6, and Cr3Te4 compounds. *Journal of Materials Science* **1983**, *18* (2), 423-429.

(120) Ipser, H.; Komarek, K. L.; Klepp, K. O. Transition metal-chalcogen systems viii: The Cr-Te phase diagram. *Journal of the Less Common Metals* **1983**, *92* (2), 265-282.

(121) Liu, L.; Wu, J.; Wu, L.; Ye, M.; Liu, X.; Wang, Q.; Hou, S.; Lu, P.; Sun, L.; Zheng, J. Phase-selective synthesis of 1T′ MoS2 monolayers and heterophase bilayers. *Nature materials* **2018**, *17* (12), 1108-1114.

(122) Yu, Y.; Nam, G.-H.; He, Q.; Wu, X.-J.; Zhang, K.; Yang, Z.; Chen, J.; Ma, Q.; Zhao, M.; Liu, Z. High phase-purity 1T′-MoS2-and 1T′-MoSe2-layered crystals. *Nature chemistry* **2018**, *10* (6), 638-643.

(123) Chen, Y.; Lai, Z.; Zhang, X.; Fan, Z.; He, Q.; Tan, C.; Zhang, H. Phase engineering of nanomaterials. *Nature Reviews Chemistry* **2020**, *4* (5), 243-256.

(124) Nunez, M.; Freitas, D. C.; Gay, F.; Marcus, J.; Strobel, P.; Aligia, A. A.; Nunez-Regueiro, M. Orbital Kondo effect in V-doped 1T-CrSe2. *Physical Review B* **2013**, *88* (24), 245129.

(125) Block, T.; Tremel, W. Large magnetoresistance at room temperature in the off-stochiometric chalcogenide Cr0. 92Te. *Journal of alloys and compounds* **2006**, *422* (1-2), 12-15.

(126) Knöner, S.; Zielke, D.; Köhler, S.; Wolf, B.; Wolf, T.; Wang, L.; Böhmer, A.; Meingast, C.; Lang, M. Resistivity and magnetoresistance of FeSe single crystals under helium-gas pressure. *Physical Review B* **2015**, *91* (17), 174510.

(127) Kamihara, Y.; Watanabe, T.; Hirano, M.; Hosono, H. Iron-based layered superconductor La [O1-xFx] FeAs (x= 0.05−0.12) with Tc= 26 K. *Journal of the American Chemical Society* **2008**, *130* (11), 3296-3297.

(128) Wang, D.; Kong, L.; Fan, P.; Chen, H.; Zhu, S.; Liu, W.; Cao, L.; Sun, Y.; Du, S.; Schneeloch, J. Evidence for Majorana bound states in an iron-based superconductor. *Science* **2018**, *362* (6412), 333-335.

(129) Zhang, P.; Yaji, K.; Hashimoto, T.; Ota, Y.; Kondo, T.; Okazaki, K.; Wang, Z.; Wen, J.; Gu, G.; Ding, H. Observation of topological superconductivity on the surface of an iron-based superconductor. *Science* **2018**, *360* (6385), 182-186.

(130) Kordyuk, A. Iron-based superconductors: Magnetism, superconductivity, and electronic structure. *Low temperature physics* **2012**, *38* (9), 888-899.

(131) Panfilov, A.; Pashchenko, V.; Grechnev, G.; Desnenko, V.; Fedorchenko, A.; Bludov, A.; Gnatchenko, S.; Chareev, D.; Mitrofanova, E.; Vasiliev, A. Interrelation of superconductivity and magnetism in FeSe1−xTex compounds. Pressure effects. *Low temperature physics* **2014**, *40* (7), 615-620.

(132) Tranquada, J. M.; Xu, G.; Zaliznyak, I. A. Magnetism and superconductivity in Fe1+ y Te1− xSex. *Journal of Physics: Condensed Matter* **2020**, *32* (37), 374003.

(133) McLaughlin, N. J.; Wang, H.; Huang, M.; Lee-Wong, E.; Hu, L.; Lu, H.; Yan, G. Q.; Gu,

G.; Wu, C.; You, Y.-Z. Strong Correlation Between Superconductivity and Ferromagnetism in an Fe-Chalcogenide Superconductor. *Nano Letters* **2021**, *21* (17), 7277-7283.
(134) Hu, D.; Ye, C.; Wang, X.; Zhao, X.; Kang, L.; Liu, J.; Duan, R.; Cao, X.; He, Y.; Hu, J. Chemical Vapor Deposition of Superconducting FeTe1–x Se x Nanosheets. *Nano Letters* **2021**, *21* (12), 5338-5344.

Table 1. Summary of the CVD synthesis of magnetic 2D TMCs.

	Materials	Precursors	Substrate	Temperature (°C)	Carrier Gas (sccm)	Growth Time (min)	Phase	Magnetic Properties	Ref.
Cr_mX_n	Cr_2S_3	$CrCl_2$ and S powders	mica	830	Ar: 50	20	rhombohedral	antiferromagnetic	[55]
	Cr_2S_3	Cr, NaCl, and S powders	mica	700 ~ 950	Ar: 80	10 ~ 20	rhombohedral	ferrimagnetic	[41]
	Cr_2S_3	$CrCl_3$, NaCl, and S powders	mica	750	Ar: 120 H_2: 50	5 ~ 40	rhombohedral	ferrimagnetic	[50]
	CrSe	$CrCl_3$ and Se powders	mica	735	Ar: 100 H_2: 10	10 ~ 30	hexagonal	ferromagnetic	[52]
	$CrSe_2$	$CrCl_3$ and Se powders	SiO_2/Si, WSe_2	700 ~ 720	Ar: 100 H_2: 2	8	trigonal	ferromagnetic	[40]
	CrTe	$CrCl_3$, NaCl, and Te powders	SiO_2/Si	675 ~ 750	Ar: 100 H_2: 10	3	hexagonal	ferromagnetic	[54]
	$Cr_{1.5}Te_2$	$CrCl_3$ and Te powders	SiO_2/Si	750	Ar: 25	/	monoclinic	ferromagnetic	[84]
	Cr_2Te_3	$CrCl_3$ and Te powders	SiO_2/Si	750	Ar: 25	0	trigonal	ferromagnetic	[56]
	Cr_2Te_3	$CrCl_3$, NaCl, and Te powders	mica	850	150: Ar and H_2 in total	/	hexagonal	ferromagnetic	[57]
	Cr_5Te_8	$CrCl_2$ and Te powders	mica	600 ~ 900	Ar: 50 H_2: 20	10	trigonal	ferromagnetic	[58]
	Cr_5Te_8	$CrCl_3$ and Te powders	SiO_2/Si	670 ~ 730	Ar: 100 H_2: 5	2	trigonal/monoclinic	ferromagnetic	[53]

	$CrTe_2$	$CrCl_2$ and Te powders	SiO_2/Si	710	Ar: 200 H_2: 1	2	trigonal	ferromagnetic	[51]
Fe_mX_n	FeTe	$FeCl_2$ and Te powders	SiO_2/Si	500 ~ 600	Ar: 100 H_2: 10	10	tetragonal/hexagonal	ferromagnetic (hexagonal) /antiferromagnetic (tetragonal)	[39]
	Fe_xGeTe_2	$FeCl_2$, KI, Ge, and Te powders	SiO_2/Si	550 ~ 600	Ar: / H_2: 5	1	rhombohedral	ferromagnetic	[74]
	Fe_7Se_8	$FeCl_2$ and Se powders	mica	560	Ar: 100 H_2: 10	5 ~ 50	hexagonal	ferromagnetic	[42]
	FeTe	$FeCl_2$ and Te powders	mica, SiO_2/Si	550 ~ 650	100: 10% H_2 in Ar	5	tetragonal/hexagonal	ferromagnetic (hexagonal)	[70]
	$FeTe_2$	$FeCl_2$ and Te powders	SiO_2/Si	520 ~ 550	50: 3% H_2 in Ar	30	orthorhombic	not mentioned	[71]
	FeTe	$FeCl_2$ and Te powders	SiO_2/Si	600 ~ 750	Ar: 45 H_2: 5	1 ~ 10	tetragonal/hexagonal /superlattice	linear magnetoresistance (hexagonal)	[67]
	FeTe	$FeCl_2 \cdot 4H_2O$ powder	SiO_2/Si	520 ~ 620	Ar: 25 H_2: 20	15	tetragonal/hexagonal	not mentioned	[68]
	$FeSe_2$	FeO/NH_4Cl and Se powders	mica	750	Ar: 104 H_2: 6	15	hexagonal	negative magnetoresistance	[72]
	$FeTe_2$	$FeCl_3$ and Te powders	mica	720	Ar: 220 H_2: 20	15	hexagonal	linear magnetoresistance	[69]
V_mX_n	V_5S_8	VCl_3 and S powders	SiO_2/Si	600	/	/	monoclinic	antiferromagnetic, spin-glass-like state, ferromagnetic	[44]
	VSe_2	V_2O_5/NH_4Cl and Se powders	SiO_2/Si	400 ~ 500	Ar: 90 H_2: 10	20	trigonal	weak antilocalization effect	[45]

	VTe_2	V_2O_5/NH_4Cl and Te powders	SiO_2/Si	750	Ar: 270 H_2: 30	20	trigonal	Kondo effect	[103]
Mn_mX_n	MnTe	$MnCl_2$/NaCl powders	mica	500	Ar: 200 H_2: 50	15	hexagonal	antiferromagnetic	[46]

For Table of Contents Only